Corrosion analysis and performance investigation of hybrid MXene/C-dot Nanofluid-Based direct absorption solar collector

Link to publication record in Ulster University Research Portal

Document Version
Publisher's PDF, also known as Version of record

Corrosion analysis and performance investigation of hybrid MXene/C-dot Nanofluid-Based direct absorption solar collector

Sreehari Sreekumar [a],[*], Jyothis Shaji [b], Gaius Cherian [b], Shijo Thomas [b], Jayanta Deb Mondol [a], Nikhilkumar Shah [a]

[a] Centre for Sustainable Technologies (CST), Belfast School of Architecture and the Built Environment, Ulster University, York St, Belfast BT15 1ED, Northern Ireland, UK
[b] School of Materials Science and Engineering, National Institute of Technology Calicut, 673601 Kerala, India

A B S T R A C T

Nanofluids having exceptional thermo-optical characteristics can enhance the performance of direct absorption solar collectors (DASC). Conventional nanofluids have either high optical properties or thermal properties. In this study, carbon quantum dot (C-dot) nanomaterial with high stability and optical absorption along the UV range, and MXene nanoparticles with high thermal conductivity and absorption along visible and near-infrared (NIR) spectral range was selected for synthesizing a hybrid nanomaterial with synergistic thermo-optical properties. Hybrid MXene/C-dot nanofluid exhibits higher stability, thermal conductivity, and complementary absorption properties of individual nanomaterials. A two-step method was used for the synthesis of nanofluids using water as the base fluid. Thermal conductivity, UV–Vis-NIR spectroscopy, and stability analysis were conducted on nanofluids, and the concentration was optimized for corrosion study and application in direct absorption parabolic trough collector (DAPTC). Optimised concentrations of C-dot, MXene, and hybrid nanofluids were 0.15 wt%, 0.1 wt% and 0.15 wt%, respectively. The corrosion study states that copper electrodes dipped in the hybrid nanofluid exhibited the least corrosion rate of 0.6 mm/year with an anticorrosion efficiency of 64.5 % over DI water. Thermal efficiency and entropy generation in the system with different HTFs were measured and compared with that of the base fluid. The study shows that C-dot and MXene/C-dot nanofluids were producing the highest efficiencies of 50.5 % and 47.5 % at a flow rate of 1.2 lpm. This study shows that hybrid MXene/C-dot nanofluid exhibited exceptional thermal stability, reduced corrosion effects, and considerable enhancement in photothermal conversion efficiency of the DASC.

1. Introduction

The energy crisis and carbon emissions are the main challenges faced by humanity at present. One of the effective methods to tackle these crises and reduce their impact on the environment is the large-scale adoption of renewable energy [1]. Effective deployment of renewable energy resources could reduce the dependency on conventional fossil fuels [2]. Of all the renewable energy sources, solar energy holds greater significance due to its abundance, ease of access, and flexibility in terms of energy conversion. Numerous photovoltaic [3], photothermal [4], photochemical [5], photobiological [6], and hybrid solar energy conversion devices [7] have been developed over the years. Photothermal systems effectively converts solar energy to thermal energy for various heating purposes. The thermal efficiency of the photothermal collectors

needs to be improved by reducing the heat loss from the system.

Photothermal collectors are categorized into surface absorption and direct absorption collectors, based on the method of solar radiation absorption. Surface absorption solar collectors (SASC) use an absorber material (black paint, spectral selective absorber coatings, etc) to convert the incident radiation to thermal energy which gets transferred to the working medium through heat transfer [8]. In a DASC the incident solar radiation passes directly through the working fluid. This fluid with high photothermal conversion efficiency will aid in the energy conversion process [9]. An intermediary absorber surface is not required for DASC as the fluid could be directly used for heating application. Conventional heat transfer fluids are better suited for SASCs due to their thermophysical properties. However, they find it difficult to be applicable in DASCs, due to lower optical absorption capability [10]. To overcome this issue, nanofluids with fine-tuned optical properties can be

* Corresponding author.
  E-mail address: s.sreekumar@ulster.ac.uk (S. Sreekumar).

Nomenclature

Parameters

A	Aperture area [m^2]
C_p	Specific heat [$J\ kg^{-1}\ K^{-1}$]
C_r	Corrosion rate [$mm\ year^{-1}$]
ew	Equivalent weight [$g\ equivalent^{-1}$]
I	Solar radiation intensity [Wm^{-2}]
I_{corr}	Corrosion current [A]
k	Thermal conductivity [$Wm^{-1}K^{-1}$]
$\dot{m}$	Mass flow rate [kgs^{-1}]
Q_{loss}	Heat loss [W]
Q_s	Incident solar energy [W]
Q_u	Useful heat gain [W]
R_p	Polarization potential [V]
S_m	Solar-weighted absorption [Wnm^{-1}]
S_{gen}	Entropy generation [WK^{-1}]
t	Time [s]
T	Temperature [℃]
T_s	Temperature of the sun [℃]
ΔT	Instantaneous temperature difference [℃]
y	Penetration depth [m]

Greek Symbol

ρ	Density [kgm^{-3}]
φ	Weight percentage [%]
β	PV cell temperature coefficient
β_a	Anodic slope
β_c	Cathodic slope
η	Efficiency [%]
η_{cr}	Anticorrosion efficiency [%]
μ	Viscosity [$kgm^{-1}s^{-1}$]
λ	Wavelength [nm]
δ	Uncertainty [%]

Abbreviations

AM	Air mass
C-dot	Carbon quantum dot
CuO	Copper oxide
DAPTC	Direct absorption parabolic trough collector
DASC	Direct absorption solar collector
EIS	Electrochemical impedance spectroscopy
EVA	Ethyl vinyl acetate
EG	Ethylene glycol
FVM	Finite volume method
HTC	Heat transfer coefficient
HTF	Heat transfer fluid
MWCNT	Multi-walled carbon nanotube
N-DAPTC	Nanofluid-based direct absorption parabolic trough collector
NIR	Near-infrared
OCP	Open circuit potential
SASC	Surface absorption solar collector
SWAF	Solar-weighted absorption fraction
UV	Ultraviolet

Subscript

amb	Ambient
in	Inlet
bf	Base fluid
ex	Exergy
f	Fluid
nf	Nanofluid
np	Nanoparticle
out	Outlet
ref	Reference
sol	Solar
th	Thermal

used in DASCs.

Numerous nanofluids have been synthesized using metals, metal oxides, carbides, nitrides, and carbon-based nanomaterials, for application in DASCs [11]. Based on the homogeneity of nanofluids, they are further categorized into monocomponent nanofluids (consisting of one nanomaterial) or multi-component/hybrid nanofluids (consisting of more than one nanomaterial) in the base fluid [9]. Abundant research has already been published on the synthesis, characterization and application of monocomponent nanofluids in DASCs [12–15]. Zhu et al. [16] performed photothermal characterization study on coal and plant derived carbon soot nanofluids. The study reports that plant soot nanofluid exhibited photothermal efficiency of about 56 % with an improvement of around 10 % over coal soot-based nanofluid. Balakin and Struchalin [17] synthesized a low-cost eco-friendly nanofluid from coffee. The study reveals that an extinction coefficient of 300 m^{-1} was achieved with 0.2 wt% nanofluid. Jiang et al. [18] synthesized MXene nanofluid with high photothermal conversion efficiency for the solar membrane distillation process. Monocomponent nanofluid is limited in its absorption capability due to a narrow solar spectral absorption band. Hybrid nanofluids overcome this disadvantage, due to a broader absorption band originating from the synergistic properties of the component materials [19]. Hence, hybrid nanofluid finds more flexible in tuning their optical absorption property. Wen et al. [20] developed ZrC/TiN nanofluid for direct absorption applications. The study states that nanofluid was able to achieve about 73.7 % photothermal efficiency. Yu et al. [21] synthesized Ag@Fe$_3$O$_4$ core–shell nanofluids. Enhancement in photothermal efficiency as high as 21.52 % was reported.

Researchers have investigated the application of nanofluids in different types of DASCs. Flat plate collectors (FPC) and concentrating collectors are the most widely adopted solar collectors. Again, the research in the field of nanofluid-based direct absorption flat plate collectors is almost saturated. Parabolic trough collectors (PTCs) and compound parabolic trough collectors (CPCs) are the most common concentrating type of DASCs. Numerous monocomponent nanofluids have been used in DAPTCs. Performance investigation on carbon soot-based DAPTC was carried out by Sreekumar et al. [22] and a maximum thermal efficiency of 50 % was reported. Heyhat et al. [23] reported that the usage of metal foam and CuO nanofluid in DAPTC has enhanced the thermal efficiency of the system by 60 % as that with DI water and metal foam.

The major drawback faced by nanofluids are the colloidal stability. Nanofluids with broadband optical absorptivity and higher stability are desirable for DASCs. Numerous research have reported the exceptional stability and photothermal efficiency of carbon quantum dot nanofluids (C-dot). A highly stable C-dot nanofluid with high optical absorptivity was synthesized by Joseph et al. [24] for application in DAPTC. The study reveals that the system achieves a maximum thermal efficiency of 73.4 % with a C-dot nanofluid. Microwave synthesis derived ultra-stable C-dot nanofluid was developed by Chen et al. [25]. The study reports that nanofluid achieved a photothermal efficiency of about 81 %. The stability of the fluid was found to be unaffected by fluid temperature or solar intensity. C-dot nanofluid was found to be promising HTF for DASCs. However, the limitation faced by C-dot is poor thermal conductivity and the absorption is limited to UV–Vis wavelength range. HTFs including TiN [26], ATO [27], and MXene [28] have been reported
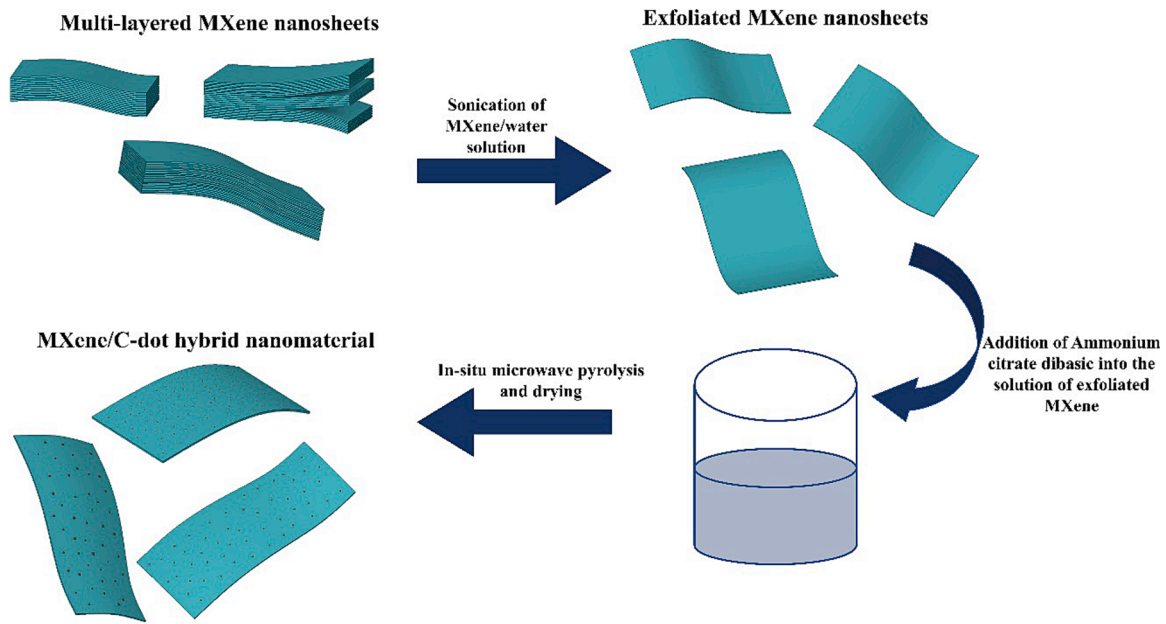
Multi-layered MXene nanosheets

Exfoliated MXene nanosheets

Sonication of MXene/water solution

Addition of Ammonium citrate dibasic into the solution of exfoliated MXene

MXene/C-dot hybrid nanomaterial

In-situ microwave pyrolysis and drying

Fig. 1. Hybrid MXene/C-dot nanomaterial synthesis methodology.

to exhibit high NIR absorption. MXene was reported to be a better thermally conducting fluid [29]. Photothermal characterization of MXene nanofluid was conducted by Qu et al. [28]. The study reported that MXene nanofluid shows considerable absorption along the spectrum, and plasmonic resonance at NIR region with an absorption peak at 810 nm. Hybrid nanofluids consisting of two or more nanomaterial with absorption peaks at different wavelength shows complementary absorption along the spectrum in comparison to monocomponent nanofluids [27].

Research on DAPTC with hybrid nanofluids are very rare in comparison to monocomponent nanofluids. Zuo et al. [4] synthesized a broadband absorbing water-based core–shell SiO$_2$@C hybrid nanofluid with surface modification induced by cellulose nanofiber. Sreekumar et al. [27] synthesized spectral selective antimony tin oxide/silver hybrid nanofluid for application in DAPTC. Experimental investigation on the collector shows that hybrid nanofluid produced thermal efficiency of 63.5 %. Joseph et al. [30] evaluated the performance of SiO$_2$/Ag-CuO hybrid plasmonic nanofluid-based DAPTC. The study reveals that the system reported a maximum photothermal efficiency of about 64.05 %. In our previous research, a novel MXene/C-dot nanocomposite material was synthesized [31]. The results from the thermo-optical characterization indicate that C-dot and MXene nanomaterials show complementary absorption along UV and Vis-NIR spectrum, respectively. An experimental investigation on the applicability of the hybrid nanofluid in a DASC could elucidate the practical feasibility of the HTF.

The literature review shows that C-dot nanofluids was found to possess higher optical absorptivity, and stability in comparison to conventional nanofluids. However, thermal conductivity and narrow absorption spectrum (UV–Vis) of C-dot is a major drawback for application in DASCs. In the meantime, MXene nanofluids exhibits better thermal properties and significant absorption along the NIR range, but comparatively lower stability. Hence, a hybrid nanofluid of C-dot and MXene could outperform the individual nanofluids due to their synergistic properties. To the best of the author's knowledge, an investigation on the optical application of MXene/C-dot hybrid nanofluid has not been conducted to date. In the present study, a MXene/C-dot hybrid nanofluid has been synthesized for application in DASC. An experimental investigation has been carried out on the DAPTC with DI water, MXene, C-dot, and MXene/C-dot hybrid nanofluids as heat transfer fluid. The concentration of nanofluid was optimized based on photothermal

efficiency, thermal conductivity, and fluid stability. The nanofluid-based DAPTC was evaluated based on energy and entropy generation analysis. Corrosion analysis of electrode in hybrid nanofluid, individual nanofluids and base fluid has also been performed. An experimental study on DAPTC with MXene/C-dot, and corrosion analysis of hybrid MXene/C-dot nanofluid has not been reported to date.

2. Materials and methods

2.1. Materials for nanofluid synthesis

Laboratory grade ammonium hydrogen citrate dibasic, C$_6$H$_{14}$N$_2$O$_7$, of 99 % purity (Sigma Aldrich) was used as the carbon source for the synthesis of C-dot nanofluid. Commercially available MXene nanosheet, Ti3C$_2$-Tx, was used in the synthesis of MXene nanofluid. The raw materials for C-dot and MXene nanofluids were used in the hybrid nanofluid synthesis.

2.2. Nanofluid synthesis methodology

C-dot nanofluid was synthesized using microwave-assisted two-step synthesis [31]. For the synthesis, 2 g of ammonium hydrogen citrate dibasic was dissolved in 10 ml of DI water by stirring at room temperature. The solution was then subjected to microwave pyrolysis for 10 min at 800 W. The pyrolyzed product was then dried in hot air at 150℃ for 5 h. The nanomaterial was then collected from the container and used to synthesise the nanofluid. A two-step method was adopted for MXene nanofluid synthesis. As purchased MXene nanoparticles were dispersed in DI water to synthesise MXene nanofluid. The synthesis method adopted for C-dot nanoparticles was modified to produce MXene/C-dot hybrid nanoparticles. During the addition of ammonium hydrogen citrate to DI water, MXene nanoparticles are also introduced. The mixture is then thoroughly mixed using a magnetic stirrer and subjected to microwave treatment and drying, as C-dot nanoparticles are synthesized. Based on the weight ratio of MXene and C-dot concentrations required in the final MXene/C-dot hybrid nanomaterial, the amount of MXene nanoparticles was adjusted in the synthesis process. The synthesis route for hybrid MXene/C-dot, as shown in Fig. 1, was adopted from our previous study [31].
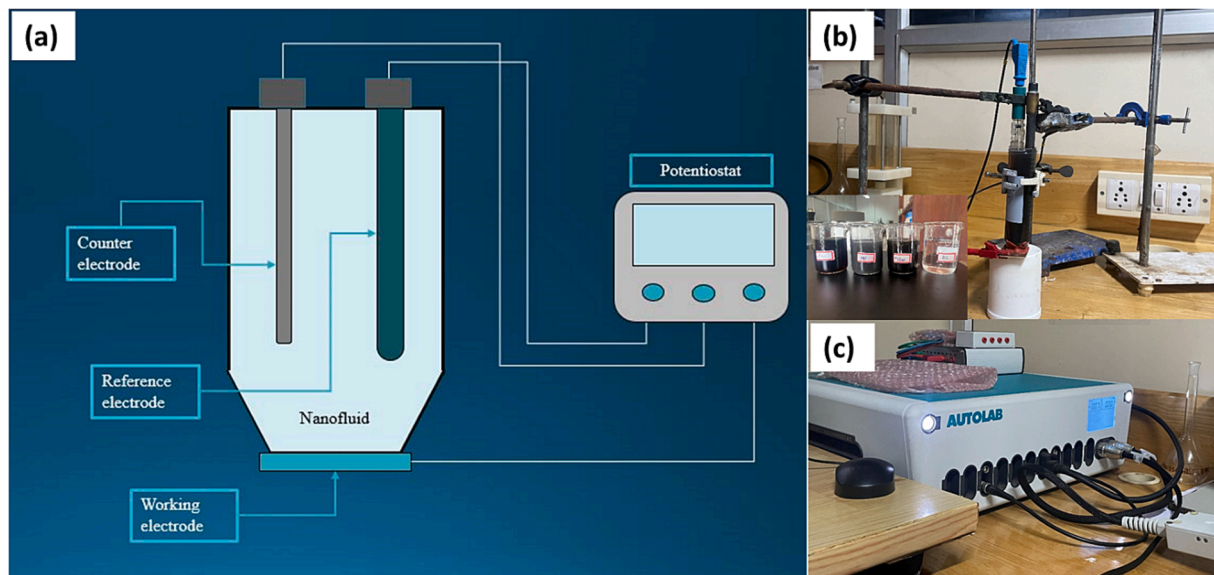
Fig. 2. (a) Schematic of corrosion cell used for electrochemical analysis (b) actual corrosion cell, and (c) electrochemical workstation.

2.3. Nanofluid concentration optimization methodology

Nanofluid concentration needs to be optimized for DASC applications. Increased scattering at the surface is a consequence of high concentrations of NPs, which in turn leads to elevated radiative losses [32]. Subsequently, heat loss is augmented due to the overheating of the nanofluid surface. Nanofluid concentration was optimized based on the optical property, thermal property, and stability of nanofluid. Photothermal application is greatly dependent on the solar absorption property of the fluid. Solar-weighted absorptivity and thermal conductivity were the respective optical and thermal properties adopted as optimization parameters. Solar-weighted absorption fraction (SWAF), S_λ, indicates the fraction of incident solar radiation that could be absorbed by the fluid. The UV–Vis-NIR spectroscopic analysis was performed using PerkinElmer Lambda 650S spectrometer. The spectral absorption values of each nanofluids, from our previous research, was used for calculating SWAF using Equation (1) [31].

$$s_m = \frac{\int_0^{\lambda max} I_{AM1.5}(\lambda)(1 - e^{-\alpha_\lambda l})d\lambda}{\int_0^{\lambda max} I_{AM1.5}(\lambda)d\lambda} \tag{1}$$

Thermal conductivity is another predominant factor that can determine the heat transport efficiency in nanofluids. A good optical fluid should also possess good thermal conductivity to effectively transfer the absorbed energy. Thermal conductivity was measured using TPS Hot Disk 2500 s.

2.4. Stability analysis methodology

Stability is the predominant factor that determines the practicability of nanofluids application in solar collectors. Even though Zeta potential analysis is the most widely adopted method to quantitatively analyse the stability of nanofluids, the method is not suitable for carbon dot nanofluids [24]. This was observed in the case of C-dot and MXene/C-dot nanofluids, which could be attributed to the high optical absorptivity of nanofluids [24]. Two quantitative and one qualitative stability analysis were performed. The quantitative techniques were to monitor the change in a physical property, before and after a period of time, during which sedimentation of nanoparticles occur (and results in the property degradation). Thermal conductivity and spectral transmittance were the two properties monitored for analysing stability. Centrifugation assisted UV–Vis spectroscopic analysis was found to be more effective for the concerned nanofluids. Stability was calculated by analysing the percentage increase in transmittance after centrifugation. The synthesised nanofluids were centrifuged at 8000 rpm for a duration of 30 min at a temperature of 20℃. UV–Vis spectroscopic analysis was conducted using Peak Instruments C7200 for studying the fluid stability. The thermal property degradation rate analysis due to stability deterioration is provided in the Supplementary data file. Visual inspection of sedimentation by nanoparticles was the qualitative method used in the study.

2.5. Corrosion analysis methodology

Corrosion analysis was performed on the optimised nanofluid concentrations using an electrochemical workstation (Metrohm Autolab PGSTAT128N). A three-electrode cell, as shown in Fig. 2, was used along with the workstation to analyse the corrosion behaviour of the nanofluids. A stable open circuit potential was obtained for each fluid after 2hrs. A copper specimen of 2 cm × 2 cm was used as the working electrode to study the corrosion mechanism of nanofluids. The specimens were mechanically polished using SiC abrasive paper down to grain size P1500. Followed by ultrasonic cleaning in acetone and washing in DI water. The effective diameter of the area exposed to the electrolyte was around 1 cm and covered an area in the range of 0.9 – 1 cm². Water being inert to ionic activity, 0.1 M NaCl solution was added to the electrolytes to induce ionic conductivity. Electrochemical spectroscopy was conducted in the frequency range of 100 kHz to 10 mHz at an amplitude of 0.01 V sinusoidal potential. Electrochemical impedance spectroscopic (EIS) analysis is a non-destructive technique to study the corrosion intensity and mechanism at the corrosion interface. Experiments on each specimen were conducted after attaining steady-state open circuit potential (OCP). The impedance spectroscopic curves were drawn based on the capacitive-resistive semicircle model [33]. The potentiodynamic polarization analysis was performed in the potential range between −0.1 V to + 0.1 V at a scan rate of 0.001 V/s. Electrochemical characterization was conducted by calculating the corrosion current (I_{corr}), corrosion potential (E_{corr}), anodic slope (β_a), cathodic slope (β_c), and corrosion rate (C_r). The intersection of anodic and cathodic Tafel slopes by the Tafel extrapolation method provides the corrosion current and corrosion potential. The corrosion rate is directly dependent on the corrosion current density. The rate of corrosion on the working electrode by different fluids could be calculated using the Stern-Geary equation given by Equation (2) [34–38].
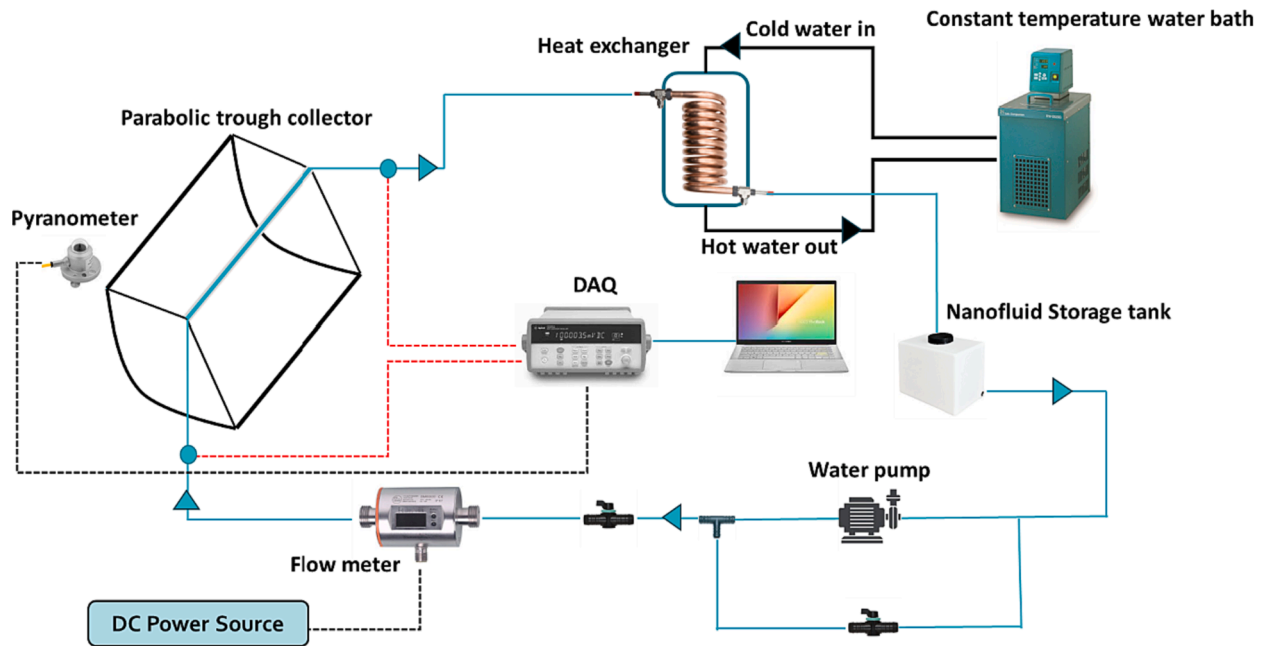
Fig. 3. Schematic diagram of the DAPTC system.

Table 1
Equipment description and specifications.

Equipment	Purpose	Model	Measuring range	Specifications
Flow meter	Measures the flow rate of nanofluid	iFM SM 6000	0.1 – 25 l/min	Ac: $\pm$ 0.5 – 0.8 % of MV Rep: 0.2 % of MV
Pyranometer	Measures the solar irradiation	Kipp & Zonen CM11	0 – 1400 Wm^{-2}	Sen: 72.8 μV/Wm^{-2} Un: $\pm$10 Wm^{-2}
Thermocouple	Measures the inlet, outlet, and ambient temperature	T-type thermocouple	–	Un: $\pm$ 0.5℃
Data logger	Records the inlet, outlet and ambient temperature, and solar radiation	Keysight E3642A	–270 to + 1820 °C	–

Ac: Accuracy; MV: Measured value; Rep: Repeatability; Sen: Sensitivity; Uncertainty: Un.

$$Corrosion\,rate, C_r = \frac{3.27 \times 10^3 \times I_{corr} \times ew}{\rho} \tag{2}$$

In Eq. (2), the equivalent weight (31.8 g per equivalent) and density (8830 kgm^{-3}) of copper electrode is represented by *ew* and ρ, respectively [37,39]. Polarization resistance was calculated using the Stern-Geary equation [35,40] given by Eq. (3).

$$Polarization\,resistance, R_p = \frac{\beta_a \times \beta_c}{2.303(\beta_a + \beta_c)I_{corr}} \tag{3}$$

The anti-corrosion performance of the samples on the working electrode was evaluated based on corrosion protection efficiency calculated using Equation (4) [36,41,42].

$$Anticorrosion\,efficiency, \eta_{cr} = \frac{I_{corr,DI} - I_{corr,NF}}{I_{corr,DI}} \tag{4}$$

A major drawback in this corrosion study of nanofluid was that the analysis is performed by keeping the fluid stationary for the period. Hence the stability of nanofluids is a significant factor, as there is the chance of nanoparticle settlement for a longer analysis time (as in this case). However, C-dot and hybrid nanofluids were having exceptional stability in stagnant conditions. But the MXene nanoparticle was found to be fully settled after 48 h and hence, the corrosion study was focussed on C-dot and MXene/C-dot nanofluids.

2.6. Experimental analysis

2.6.1. Experimental setup

The main experimental setup consists of a DAPTC as shown in Fig. 3. As observed, the working fluid is circulated in the hydraulic loop with the help of a water pump. Three different flow rates were selected for the experiment and were adjusted with the help of a flow control valve and a bypass valve. As seen from the figure, the bypass valve diverts the flow back to the pump inlet. The pipe length before and after the flowmeter was higher than 10 times the diameter of the pipe to perform accurate flow rate measurement and avoid turbulence. The temperature of the flow was measured using calibrated T-type thermocouples. The inlet temperature was maintained constant using a constant temperature water bath. The fluid exiting the DAPTC was allowed to pass through a coil heat exchanger to dissipate the heat to the cold fluid entering the heat exchanger from the water bath. The cooled fluid reaches the storage tank and was allowed to circulate through the DAPTC in a closed loop using the pump. The specifications and uncertainties of the equipment used are provided in Table 1.

2.6.2. Experimentation and analysis methodology

Performance investigation of DAPTC with nanofluids and base fluid was conducted, and a comparison was performed. The daily thermal performance of the system was monitored at constant operating parameters. A constant inlet fluid temperature was maintained throughout the experiment using the water bath. The outdoor experiments using each working fluids were conducted between 09:00 am and 04:00 pm, at a constant flow rate for each test day. The experimental study was

Table 2
Weather data recorded during the test days.

Test date	Irradiation (I) (Wm^{-2})			Ambient temperature (T_{amb}) (°C)			Ambient air velocity (ms^{-1})		
	Min.	Max.	Avg.	Min.	Max.	Avg.	Min.	Max.	Avg.
23–02-23	453.90	819.00	679.09	27.17	33.67	31.52	0.55	1.90	1.24
27–02-23	445.40	874.00	724.23	26.41	35.29	31.91	0.92	1.90	1.37
02–03-23	459.4	851	702.7	27.74	32.98	31.16	0.19	2.08	1.20
08–03-23	465.00	858.00	712.94	28.82	35.12	32.72	0.67	2.10	1.33
09–03-23	338.90	976.00	721.05	27.00	35.02	31.92	0.21	2.29	1.13
13–03-23	429.90	839.00	689.28	29.63	34.77	32.55	0.12	2.45	1.44
14–03-23	416.80	787.50	644.19	29.61	35.01	33.01	0.22	2.57	1.42
15–03-23	410.80	820.00	652.74	29.93	34.06	32.58	0.43	2.42	1.39
16–03-23	440.50	827.00	674.96	28.43	33.24	31.75	0.56	2.29	1.44
09–04-23	454.70	896.00	699.49	29.60	35.00	32.96	0.40	2.57	1.47
10–04-23	516.70	901.00	747.79	28.05	33.46	31.87	1.03	2.46	1.63
11–04-23	283.60	999.00	774.35	28.37	34.33	32.68	0.98	2.68	1.81

performed on the system with four different working fluids and was performed at three different flow rates. The data logging interval was set as 1 sec, and the average value at 15 min was used to perform the efficiency calculations. The flow rate was varied in the range of 0.2 to 1.2 l/min. The thermal efficiency of the DAPTC was analysed using basic energy balance equations applied to the solar collector. The daytime was selected such that the PTC was able to concentrate the direct solar irradiation received on the absorber tube, throughout the day. The thermal energy gained by the fluid, Q_u, through photothermal conversion was calculated using Equation (5). The total incident solar energy received by the PTC (Q_s) was calculated as shown in Equation (6). The instantaneous thermal efficiency of the system, η_{th}, was calculated as the fraction of useful thermal energy gained from the total incident solar radiation, as shown in Equation (7).

$$Q_u = m_f C_{p,f}(T_{out} - T_{in}) \tag{5}$$

$$Q_s = A.I \tag{6}$$

$$\eta_{th} = \frac{Q_u}{Q_s} = \frac{m_f C_{p,f}(T_{out} - T_{in})}{A.I} \tag{7}$$

In the above equations, A, I, m_f, $C_{p,f}$, T_{in}, and T_{out} represents the aperture area of the collector, incident radiation intensity, mass flow rate, specific heat of fluid, and, inlet and outlet temperatures of the fluid, respectively. Second law analysis was conducted to calculate the thermodynamic irreversibility due to heat loss. Hence, entropy generation (S_{gen}) in the system was calculated during the operational hours using Eqs. (8) and (9), as defined by Bejan [43]. The heat lost to the ambient (Q_{loss}) was evaluated for the entropy generation analysis as shown in Equation (9). The final entropy generation equation for the PV/T reduces to Eq. (10).

$$S_{gen} = m_f C_{p,f} \ln\left(\frac{T_{out}}{T_{in}}\right) - \frac{Q_s}{T_s} + \frac{Q_{loss}}{T_{amb}} \tag{8}$$

$$Q_{loss} = Q_s - m_f C_{p,f}(T_{out} - T_{in}) \tag{9}$$

$$S_{gen} = m_f C_{p,f} \ln\left(\frac{T_{out}}{T_{in}}\right) - \frac{IA}{T_s} + \frac{IA - m_f C_{p,f}(T_{out} - T_{in})}{T_{amb}} \tag{10}$$

The surface temperature of the sun, T_s, was assumed to be a constant and the value was taken to be 5800 K.

2.6.3. Weather data for Calicut

The meteorological data for Calicut (11.32°N, 75.93°E) was monitored using a weather station and was monitored using an in-house program. Solar radiation, wind speed, and ambient temperatures recorded by the instrument were used for analysis. Solar radiation was recorded using an industrial standard pyranometer with an accuracy of ± 5 Wm^{-2}. A vane-type anemometer (accuracy of ± 5 %) was used for recording wind velocity. Data from twelve typical days with a clear sky and having steady average solar irradiation during February, March, and April 2023, were selected for the experimental study. The daily average solar radiation received during these days varied from 733.69 Wm^{-2} to 833 Wm^{-2}. The maximum, minimum, and average values of the weather parameters that was recorded during the operational hours of the test days were tabulated as shown in Table 2.

2.6.4. Uncertainty analysis

The uncertainties associated with the measurement of experimental data were calculated using the Moffat method [44]. Equation (11) describes the general formula for calculating the uncertainty associated with a dependent parameter y, which is a function of x_1, x_2, x_3, and x_4. Correspondingly, the uncertainty in the calculation of thermal efficiency and entropy generation was measured using Eqs. (12) and (13), respectively.

$$\delta y = \sqrt{\left(\frac{\partial y}{\partial x_1}\delta x_1\right)^2 + \left(\frac{\partial y}{\partial x_2}\delta x_2\right)^2 + \left(\frac{\partial y}{\partial x_3}\delta x_3\right)^2 + \left(\frac{\partial y}{\partial x_4}\delta x_4\right)^2} \tag{11}$$

$$\delta\eta_{th} = \sqrt{\left(\frac{\partial\eta_{th}}{\partial m_f}\delta m_f\right)^2 + \left(\frac{\partial\eta_{th}}{\partial T_{in}}\delta T_{in}\right)^2 + \left(\frac{\partial\eta_{th}}{\partial T_{out}}\delta T_{out}\right)^2 + \left(\frac{\partial\eta_{th}}{\partial G}\delta G\right)^2} \tag{12}$$

$$\delta S_{gen} = \sqrt{\left(\frac{\partial S_{gen}}{\partial m_f}\delta m_f\right)^2 + \left(\frac{\partial S_{gen}}{\partial T_{in}}\delta T_{in}\right)^2 + \left(\frac{\partial S_{gen}}{\partial T_{out}}\delta T_{out}\right)^2 + \left(\frac{\partial S_{gen}}{\partial T_{amb}}\delta T_{amb}\right)^2 + \left(\frac{\partial S_{gen}}{\partial G}\delta G\right)^2} \tag{13}$$

Uncertainty in the calculation of thermal efficiency and entropy generation was calculated to be ± 2.75 % and ± 2.95 %, respectively. As the uncertainties in the calculation fall within ± 3 %, the experimentally recorded data is assumed to be accurate [45].
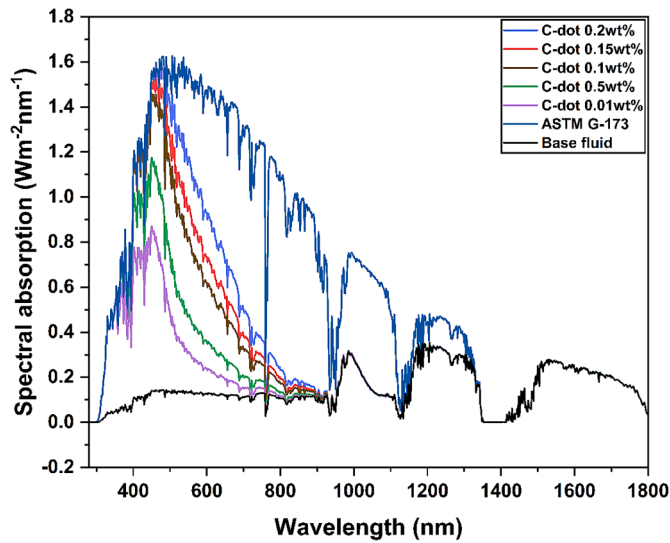
Fig. 4. Solar absorption spectra of various concentrations of C-dot nanofluid and base fluid.

3. Results and discussion

3.1. Characterization

3.1.1. Solar-weighted absorption fraction

Solar spectral absorption graphs of C-dot, MXene, and MXene/C-dot nanofluids are provided in Fig. 4, Fig. 5, and Fig. 6, respectively. Spectral absorption of C-dot nanofluid of varying concentrations as observed from Fig. 4 depicts that the absorption is predominant in the region from 280 to 460 nm. The spectral absorption spectrum of 0.2 wt% and 0.15 wt% C-dot is almost coinciding with the reference spectrum in the range 280——460 nm. However, there is a large gap between the absorption and the reference spectrum in the region 460 – 1100 nm. Fig. 5 depicts that MXene of 0.2 wt% shows the highest spectral absorption compared to other concentrations. As observed from the plot, the change in absorption was almost uniform while increasing the concentration from 0.01 to 0.1 wt%. However, the percentage increase in absorption was observed to be comparatively lower while increasing concentration above 0.1 wt%. The absorption spectrum of 0.15 % and 0.2 wt%
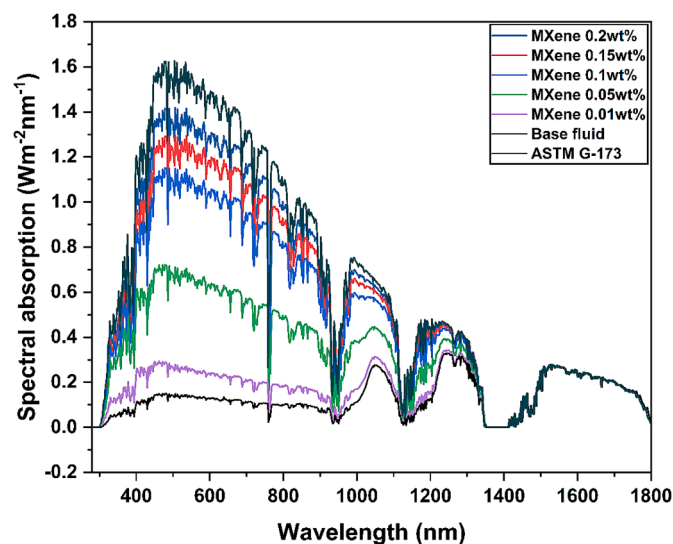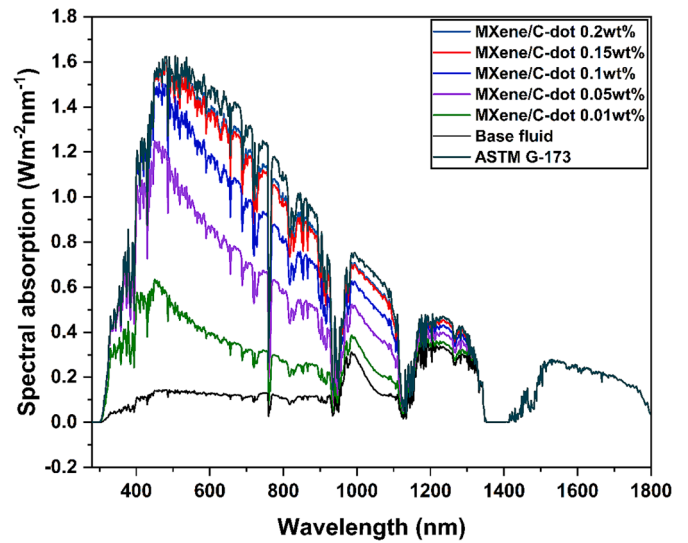

Fig. 6. Solar absorption spectra of various concentrations of MXene/C-dot nanofluid and base fluid.

0.2 wt% was almost coinciding along the wavelength range beyond 1100 nm. Solar absorption percentage enhanced by 61 and 67.8 % for 0.15 and 0.2 wt% MXene, respectively, over base fluid. Solar spectral absorption of hybrid nanofluid as visualized in Fig. 6, shows that the increase in absorption was directly proportional to the concentration of nanofluid. The absorption curve of hybrid nanofluid was observed to be the most coinciding one with the reference spectrum, in comparison to other nanofluids. Among the hybrid fluids, 0.2 wt% nanofluid exhibited around 95 % similarity with the reference solar spectrum. The absorption percentage of base fluid was calculated and was only about 22.77 %. Hence, the hybrid, MXene, and C-dot nanofluids of 0.2 wt% produced an enhancement in absorption percentage over base fluid by around 72.4, 67.8, and 37.8 %, respectively. The major reason for higher solar absorption by MXene/C-dot is the generation of surface defects on MXene due to the hybridization of C-dot [31]. These impurities has narrowed the energy band gap of the hybrid material resulting in a broader absorption range [46]. A comparative spectral absorption curve of DI water and nanofluids (0.01wt%) are shown in Fig. 7. The lowest concentration was chosen for nanofluids to exhbit the difference in the characteristics curve for spectral specific absorption.
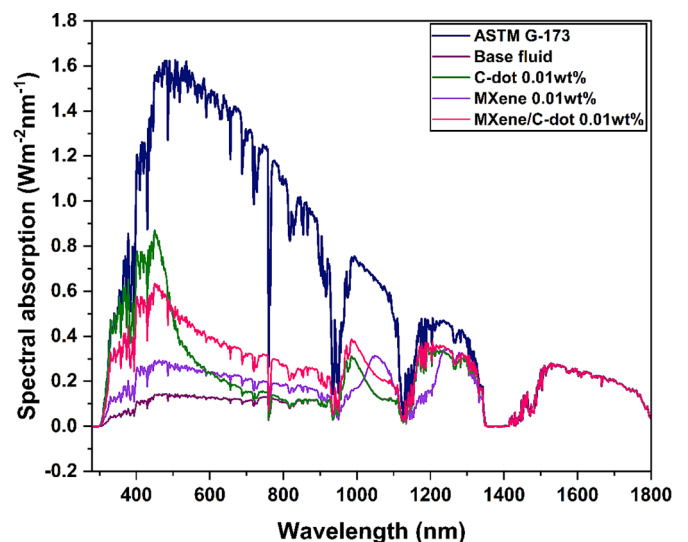

Fig. 5. Solar absorption spectra of various concentrations of MXene nanofluid and base fluid.

Fig. 7. Solar absorption spectra of all nanofluids of 0.01 wt% and base fluid.

Table 3

Thermal conductivity of nanofluids.

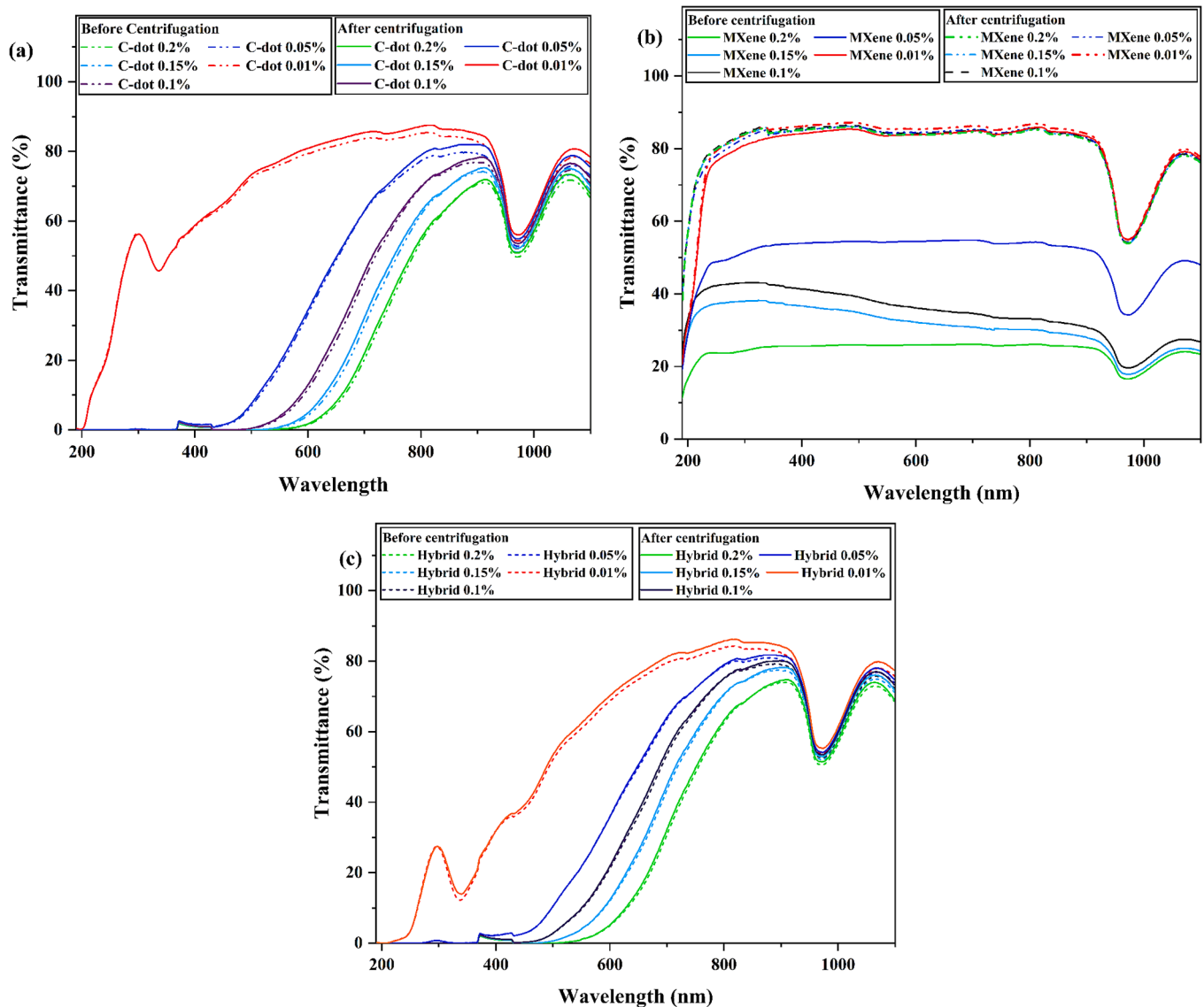| b	Thermal conductivity (Wm⁻¹K⁻¹)									
	0.01 wt%	Enh (%)	0.05 wt%	Enh (%)	0.1 wt%	Enh (%)	0.15 wt%	Enh (%)	0.2 wt%	Enh (%)
C-dot	0.624	4.17	0.630	5.17	0.646	7.85	0.681	13.68	0.705	17.6
MXene	0.628	4.84	0.638	6.51	0.665	11.01	0.707	18.03	0.721	20.36
Hybrid	0.626	4.50	0.634	5.84	0.650	8.51	0.691	15.36	0.706	17.86

Enh: Percentage enhancement (%).

Fig. 8. UV–Vis spectroscopic curves before and after centrifugation, performed on (a) C-Dot (b) MXene and (c) MXene/C-Dot nanofluid.

3.1.2. Thermal conductivity analysis

The thermal conductivity of the samples was analysed using Hot Disk 2500, which employs the transient plane source method. The thermal conductivity of all the samples was measured at the same room temperature (20℃) and results are shown in Table 3. The thermal conductivity of the C-dot nanofluid increased from 0.624 Wm⁻¹K⁻¹ at 0.01 wt% to 0.705 Wm⁻¹K⁻¹ at 0.2 wt%. Similarly, the conductivity values for MXene and hybrid nanofluid ranged between 0.628 and 0.720 Wm⁻¹K⁻¹ and 0.625 – 0.706 Wm⁻¹K⁻¹, respectively. The thermal conductivity of nanofluids was found to be proportional to the ratio of thermal conductivity of individual components of the mixture. Thermophoresis and

Brownian motion are the two other phenomenon which determines the thermal conductivity of nanofluid [31]. Detailed thermal conductivity, thermal diffusivity, and volumetric heat capacity values of the nanofluids was provided in the previous study [31].

3.1.3. Stability analysis

The UV spectrum of each nanofluid could be observed in Fig. 8. As, observed in Fig. 8 (a), the transmittance of C-dot nanofluid exhibited negligible variation before (dotted line) and after (solid line) centrifugation. The variation in transmittance was consistent with each concentration of nanofluid. The Fig. 8 (b) shows that the variation in
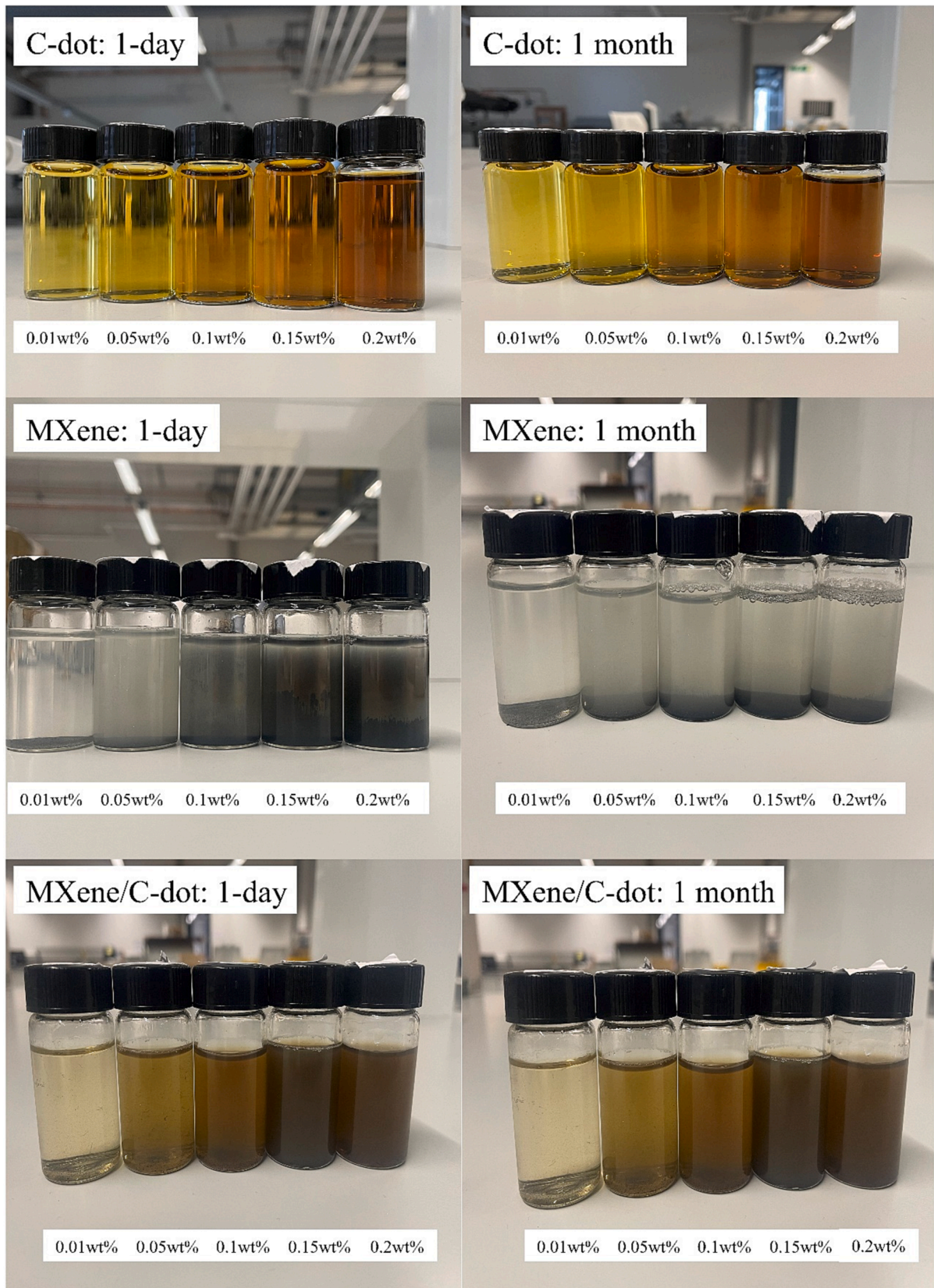
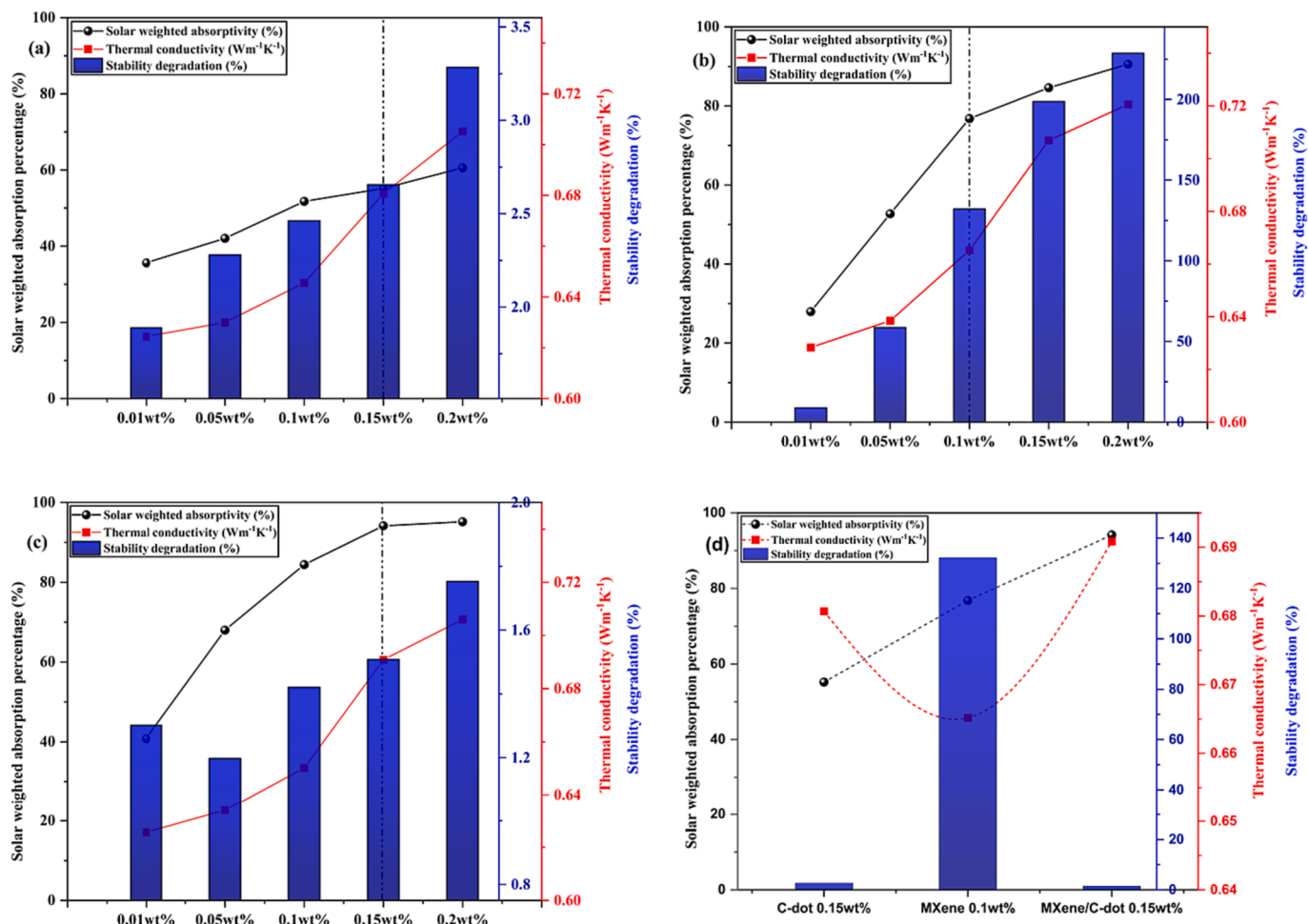**Fig. 9.** Stability analysis performed on C-dot, MXene and MXene/C-dot nanofluid.

Fig. 10. Solar weighted absorptivity, thermal conductivity, and stability degradation graphs of (a) C-Dot (b) MXene and (c) MXene/C-Dot nanofluids, and (d) optimized values of the nanofluids at optimum concentration.
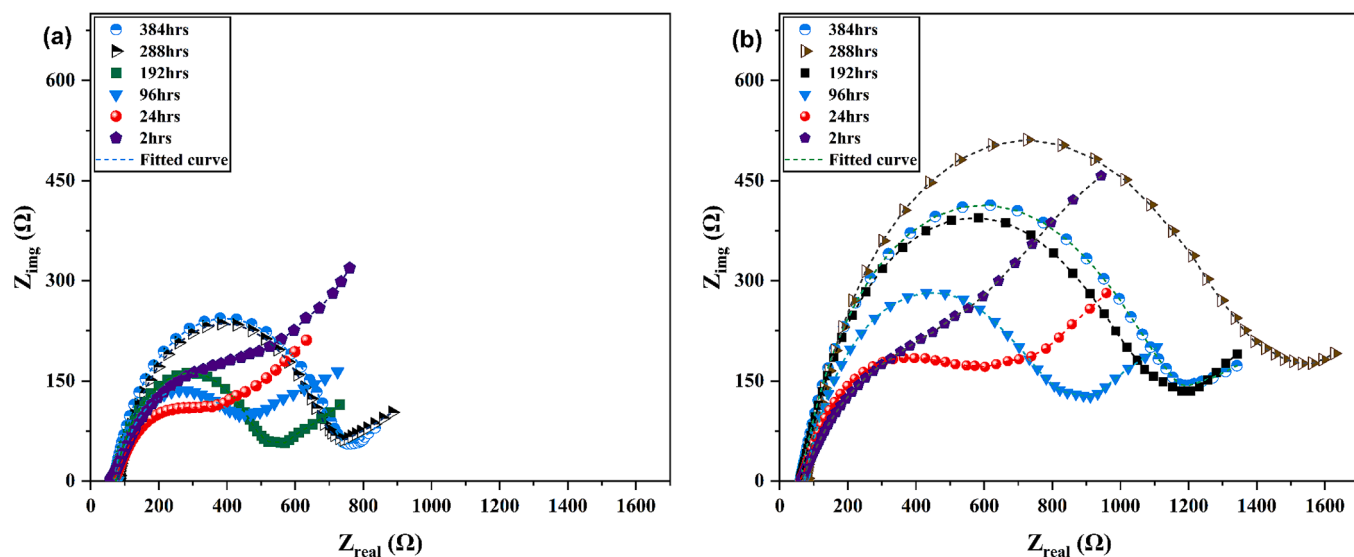

Fig. 11. Electrochemical impedance spectroscopy of (a) C-Dot, and (b) MXene/C-Dot nanofluids for 384 h.

transmittance for MXene was very significant, particularly at high concentrations, due to poor stability. Lowest degradation in transmittance was observed for 0.01 wt% MXene nanofluid. However, the remaining MXene nanofluids (0.05 – 0.2 wt%) exhibited settling of nanoparticles in the solution after centrifugation process. As observed from Fig. 8 (c), the deterioration of transmittance was lower for hybrid nanofluid. The transmittance spectra of hybrid nanofluid before and after centrifugation process was almost coinciding with each other throughout the
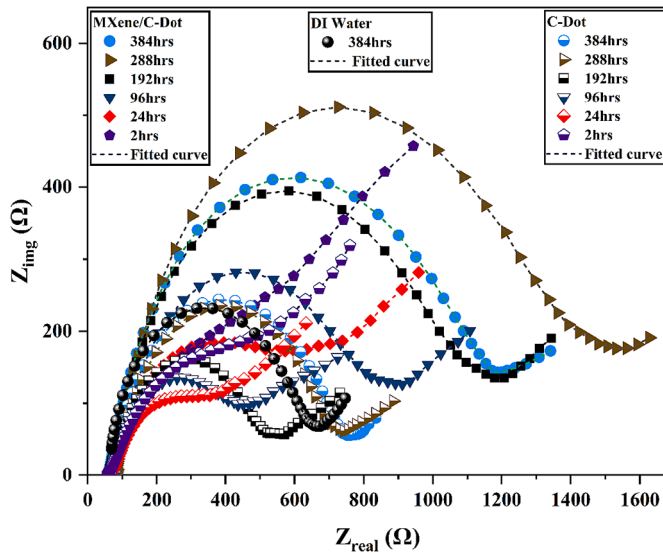
Fig. 12. EIS curves of C-Dot and MXene/C-Dot nanofluid at different exposure periods with DI water.

Fig. 14. Exposure time-dependent variation in impedance values of copper in C-Dot and MXene/C-Dot nanofluid at 0.01 Hz.

spectral range. As C-dot and MXene/C-dot hybrid nanofluid exhibits negligible sedimentation, they are found to be better candidates in terms of nanofluid stability. The qualitative analysis by visual inspection is shown in Fig. 9. The time period of one month was taken for ease of comparison. The C-dot was observed to have the longest standing hours with negligible deposition of more than two months. MXene was found to settle completely with 15 days, owing to its poor stability. MXene/C-dot nanofluids have exhibited considerable stability due to the increased concentration of C-dot in comparison to MXene.

3.2. Concentration optimization

The values of the three optimization parameters for each concentration of nanofluids are shown in Fig. 10 (a) – (c). For all the nanofluids, thermal conductivity, SWAF and stability degradation values were observed to be increasing with concentration. In the case of C-dot, SWAF at 0.15 wt% and 0.2 wt% was almost similar. Thermal conductivity variation was found to be linear. And the stability degradation was observed to be increasing steeply from 0.15 wt% onwards. Hence, 0.15 wt% was selected for the C-dot nanofluid. In, the case of MXene as seen from Fig. 10 (b), the curve of SWAF was observed to be rising steeply till
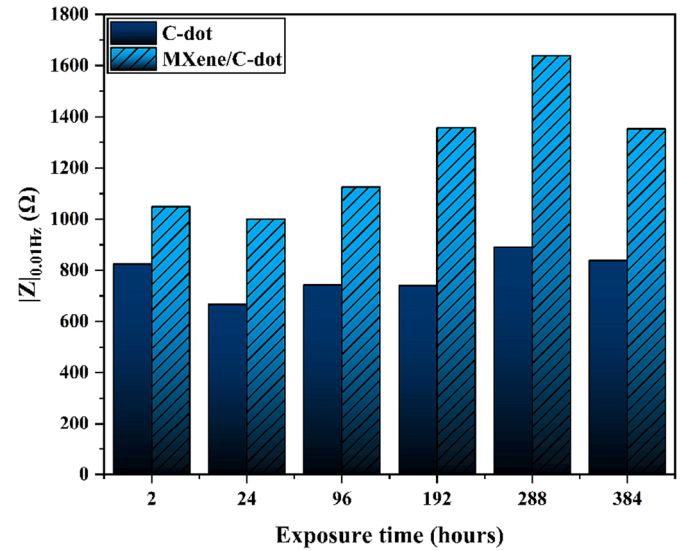
0.1 wt%. And the curve maintained a gentle slope till 0.2 wt%. However, stability was found to be decreasing for nanofluids above 0.1 wt% concentration. MXene at 0.1 wt% was thus adopted for further study, also the thermal conductivity value at that concentration was acceptable. The characteristics values of the hybrid nanofluid are provided in Fig. 10 (c). It could be inferred that the optimum concentration is 0.15 wt%, since beyond this concentration the variation in solar absorptivity and thermal conductivity is minimal, while the degradation in stability is stability is significant.

3.3. Corrosion analysis

3.3.1. Electrochemical impedance spectroscopic analysis

Nyquist plot obtained from the corrosion analysis performed on the copper electrode is shown in Fig. 11 (a) and (b). A larger semi-circle diameter indicates that the corrosion resistance of the working electrode in the medium is high [41]. The impedance spectra of the electrode in C-dot, as seen in Fig. 11 (a), were not perfect semi-circles even after 96 h of exposure, which confirmed that oxide layer formation is not uniform [47]. The diameter of the arc at 24 h of exposure decreased from that obtained after 2 h. After 24 h, all the measurements reported a
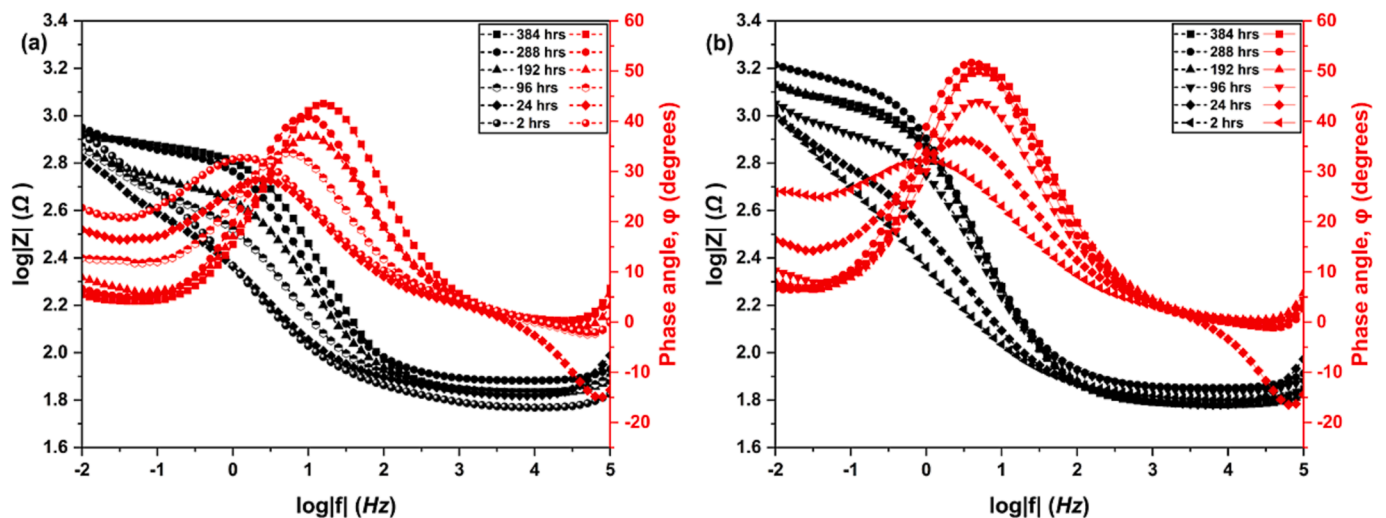

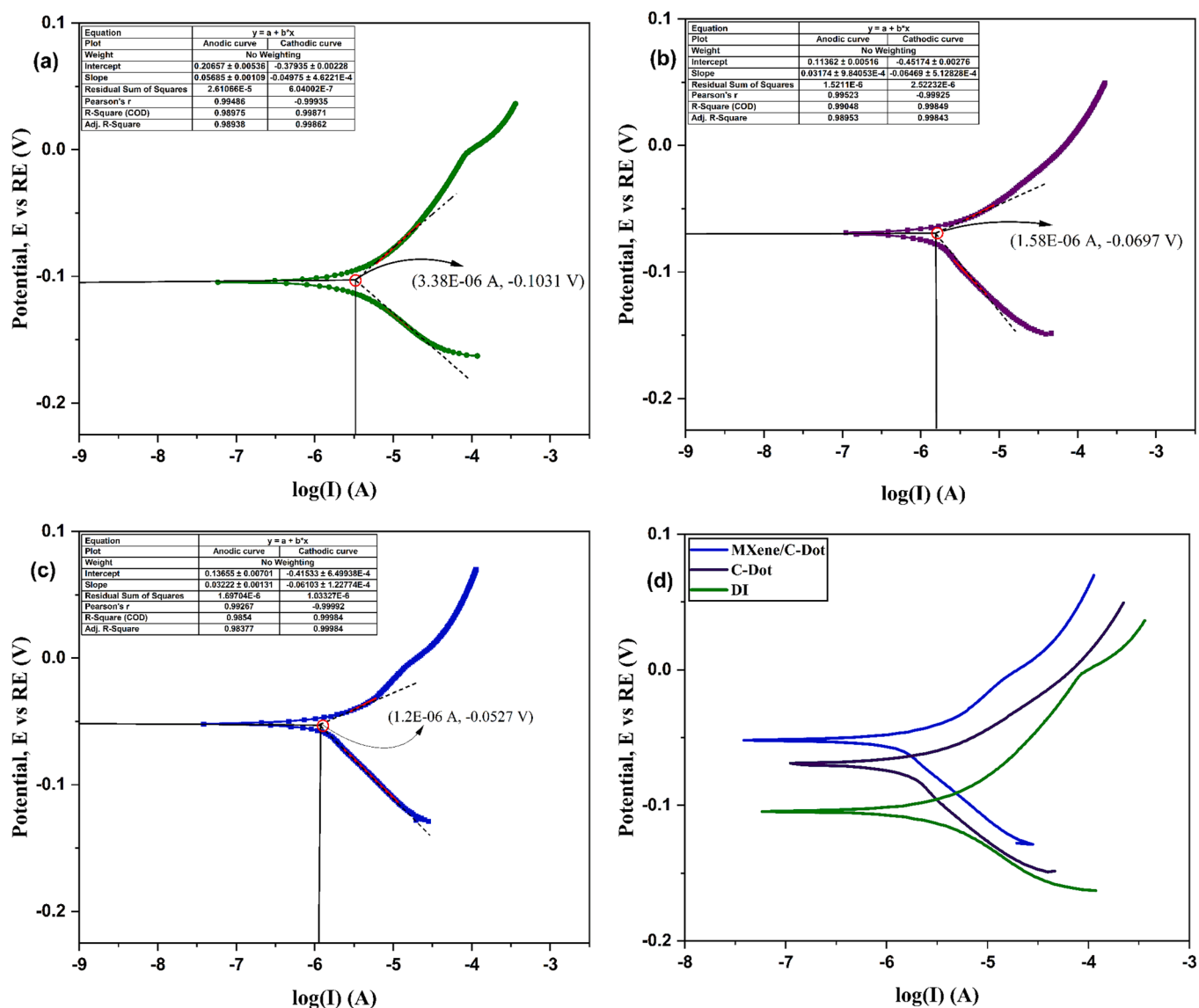**Fig. 13.** Bode plot of (a) C-Dot (b) MXene/C-Dot nanofluids for 384 h.

Fig. 15. Tafel polarization curves of (a) DI water, (b) C-Dot (c) MXene/C-Dot nanofluid showing the corrosion current and potential, and (d) superimposed Tafel curves of all fluids.

visible increment in the diameter of the semi-circle till 288 h (12th day). Finally, after 384 h (16 days) of immersion, the curve was found to be coinciding with the curve obtained after 288 h. Hence, it is inferred from the EIS of C-dot that the corrosion mechanism is not uniform. As observed in Fig. 11 (b), the EIS spectrum of hybrid nanofluid shows similarity with that of C-dot nanofluid. This indicates that the corrosion mechanism of hybrid nanofluid is predominantly dependent on the corrosion property of C-dot nanoparticles. Depressed semi-circles were observed for the measurements conducted on copper electrodes after 2 to 24 h of exposure to hybrid nanofluid. However, a homogenous oxide layer was formed on the electrode at a rate faster than that with C-dot. After 24 h, the diameter of the semi-circle increased considerably with

an increase in immersion time to 288 h. After 384 h, the impedance arc was found to be reduced in magnitude. This indicates that the coating formed on the substrate is achieving corrosion stability. The EIS analysis shows that copper electrode in hybrid nanofluid shows better corrosion resistance over that in C-dot medium.

EIS spectrum of hybrid and C-dot nanofluids for each period of the analysis is superimposed as visualised in Fig. 12. The impedance plot of DI water after 384 h is also included for comparison. Also, the capacitive arc of the C-dot was observed to be larger than that of water after 384 h. This shows that the corrosion resistance of copper in C-dot is better than that of water for longer periods. Similarly, the charge transfer resistance of the electrode in hybrid nanofluid is twice as in DI water. This indicates

Table 4
Electrochemical parameters from the polarization curve.

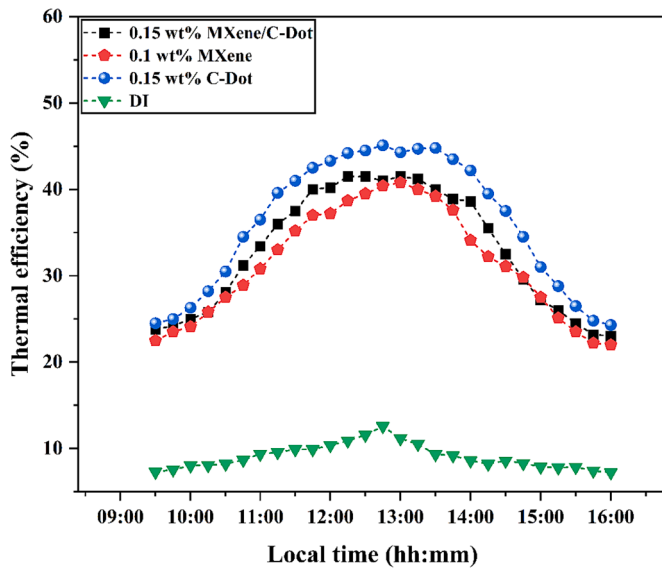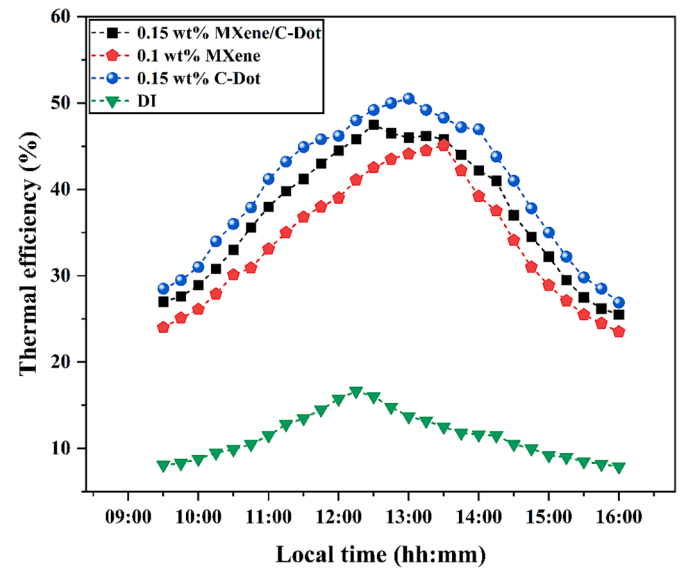| Electrolyte	E_{corr} (V)	I_{corr} (A)	J_{corr} (Acm^{-2})	β_a (V/dec)	β_c (V/dec)	R_p (Ω)	C_r(mm/year)	η_{cr}(%)
DI water	−0.1031	3.38E-06	3.377E-06	0.020	−0.049	4329.09	1.55	-/-
C-Dot	−0.0697	1.58E-06	1.765E-06	0.032	−0.449	9562.30	0.81	53.2
MXene/C-Dot	−0.0516	1.20E-06	1.32E-06	0.026	−0.061	16789.50	0.60	64.5

Fig. 16. Thermal efficiency of the DAPTC with different working fluids at a flow rate of 0.2 lpm.

Fig. 18. Thermal efficiency of the DAPTC with different working fluids at a flow rate of 1.2 lpm.

impedance over C-dot and hence a less corrosive medium.

3.3.2. Potentiodynamic polarization

The Tafel polarization curve of DI water, C-Dot, MXene, and MXene/ C-Dot nanofluid is shown in Fig. 15. The polarization curves of the electrode in MXene/C-dot and C-dot nanofluid are shifted towards the positive potential in comparison to MXene and DI water. This positive shift indicates the cathodic nature of the electrode in these nanofluids, and hence they are more resistant to corrosion. Electrochemical parameters from the Tafel polarization study such as I_{corr}, E_{corr}, β_a, β_c, C_r, and η_{cr}, are tabulated as seen in Table 4. A higher value for polarization resistance indicates higher corrosion resistance by the fluid [34]. As observed from the data, MXene/C-Dot nanofluid exhibited the highest polarization resistance of 16.7 $k\Omega$. The corrosion rate of copper in three fluids was calculated after 384 h of immersion and is given in Table 4. The results indicate that MXene/C-dot nanofluid exhibited the lowest corrosion rate of about 0.6 mm/year, followed by C-dot of about 0.81 mm/year. Copper dipped in DI water exhibited the highest corrosion rate of 1.55 mm/year. Anti-corrosion efficiency indicates the corrosion resistance offered by nanofluid over that of the base fluid. The electrochemical polarization studies show that after 384 h of immersion, the corrosion resistance of the working electrode was higher in the nanofluid medium as compared to that dipped in DI water. Hence, the corrosion resistance of DI water was taken as the reference and the corrosion inhibition efficiency of other fluids was calculated. The analysis shows that MXene/C-Dot and C-Dot nanofluid has corrosion inhibition efficiencies of about 64.5 and 53.2 %, respectively over DI water.

3.4. Performance evaluation of DAPTC

3.4.1. Thermal efficiency analysis

The variation of thermal efficiency during daytime for all the working fluids at flow rates of 0.2 lpm, 0.6 lpm, and 1.2 lpm, are shown in Fig. 16, Fig. 17, and Fig. 18, respectively. All three efficiency graphs show a similar trend. It is observed that the thermal efficiency of the system increases with time and reaches a maximum value between 12:00 pm to 1:30 pm. As inferred from Fig. 16–18, the radiation intensity also increases with time and reaches a maximum value around the above-mentioned time. Hence, as the radiation intensity increases, the parabolic reflector can concentrate more incident radiation to the absorber tube, which increases the thermal efficiency of the system. Also, as the temperature of the system increases, the heat loss to the
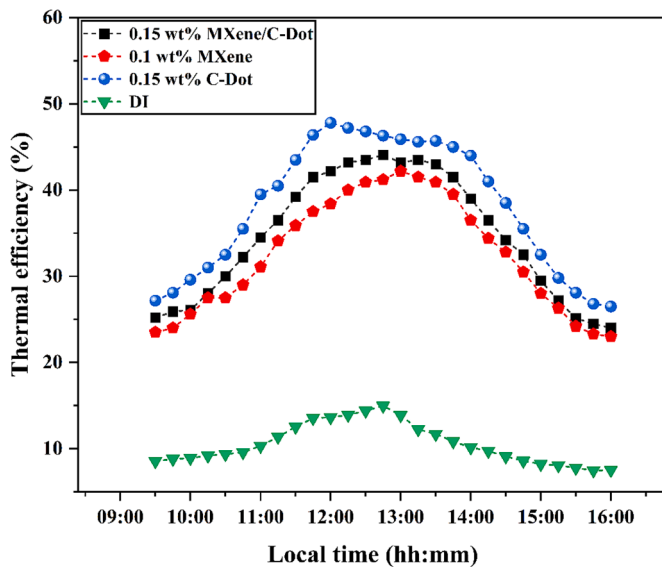

Fig. 17. Thermal efficiency of the DAPTC with different working fluids at a flow rate of 0.6 lpm.

that copper specimen in a hybrid nanofluid has twice the corrosion resistance than that of C-dot and DI water. The major reason for this phenomenon is that the anticorrosive property exhibited by the protective oxide layer, on the electrode, by MXene/C-dot is higher than that of C-dot.

The major limitation of the Nyquist plot is that the curve doesn't throw light on the frequency at which the impedance was measured. This drawback was compensated by plotting a Bode modulus and bode phase plot for C-dot and hybrid nanofluid, as shown below in Fig. 13. Corrosion resistance is directly related to impedance modulus at low frequencies [48]. The Bode modulus plot and Bode phase angle plot for C-dot as given in Fig. 13 (a), shows that the impedance modulus increased with immersion time. The impedance magnitude ($|Z|$) of C-dot was observed to be increasing at lower frequencies, and hence better corrosion resistance. The variation in impedance value of copper in a nanofluid medium measured at 0.01 Hz is shown in Fig. 14. It could be inferred that the electrode in hybrid nanofluid exhibits higher

Table 5
Performance parameter values of DAPTC with nanofluids and base fluid.

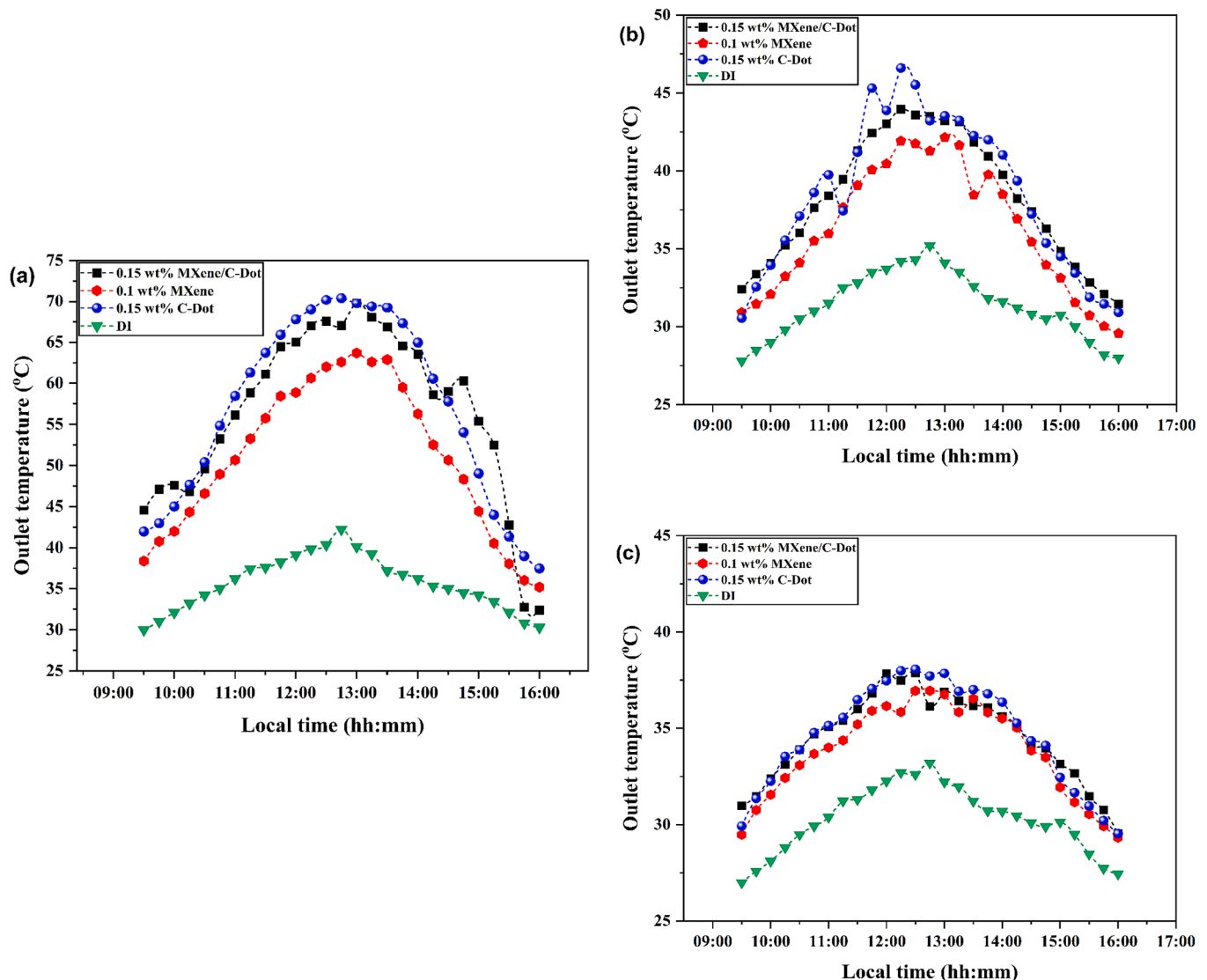| Working fluid	Thermal efficiency (%)			Outlet temperature (°C)			Entropy generation (WK^{-1})		
	Min.	Max.	Avg.	Min.	Max.	Avg.	Min.	Max.	Avg.
DI water	7.9	16.64	11.54	26.99	42.24	32.41	2.08	4.00	3.23
MXene	22.00	45.10	32.70	29.33	63.68	40.29	1.91	3.78	3.01
C-Dot	24.30	50.50	38.04	29.54	70.41	43.28	1.58	4.43	3.24
MXene/C-Dot	23.00	47.50	34.98	29.55	69.78	43.01	1.30	4.50	3.39

Fig. 19. Outlet temperature of DAPTC with different working fluids at a flow rate of (a) 0.2 lpm, (b) 0.6 lpm, and (c) 1.2 lpm.

surroundings increases correspondingly. However, as radiation intensity increased the DAPTC was able to compensate for the heat loss, there was considerable enhancement in the thermal efficiency.

The thermal efficiency of the PTC was found to be lowest at 0.2 lpm and highest at 1.2 lpm. As the flow rate decreases, the heat lost by the fluid to the surroundings increases, thereby reducing the thermal efficiency of the system. At a flow rate of 1.2 lpm, the heat transfer fluid takes lesser time to cover the length of the receiver tube, and hence lesser heat loss. As seen in Fig. 16, the C-dot nanofluid produced the highest thermal efficiency, in comparison to other fluids. At 0.2 lpm, the highest thermal efficiency achieved by the system with C-dot, MXene/C-dot, MXene, and DI water is 45.1, 41.5, 40.8, and 12.57 %, respectively.

The highest efficiency enhancement of about 35.4 % was obtained with C-dot nanofluid, in comparison with water. The corresponding enhancements produced with MXene/C-dot and MXene nanofluids were 30.68 % and 29.64 %, respectively. Apart from photothermal efficiency, various factor including photoluminescence and scattering could also be attributed to this variation in efficiency.

A similar trend in thermal efficiency could be observed in Fig. 17, in which the C-dot nanofluid outperformed the remaining fluids. C-dot nanofluid exhibited the highest thermal efficiency of 47.8 % at noon and produced an enhancement of about 34.16 % over DI water. The highest thermal efficiency of the system with base fluid was only 14.4 %. MXene/C-dot and MXene nanofluids were found to be having
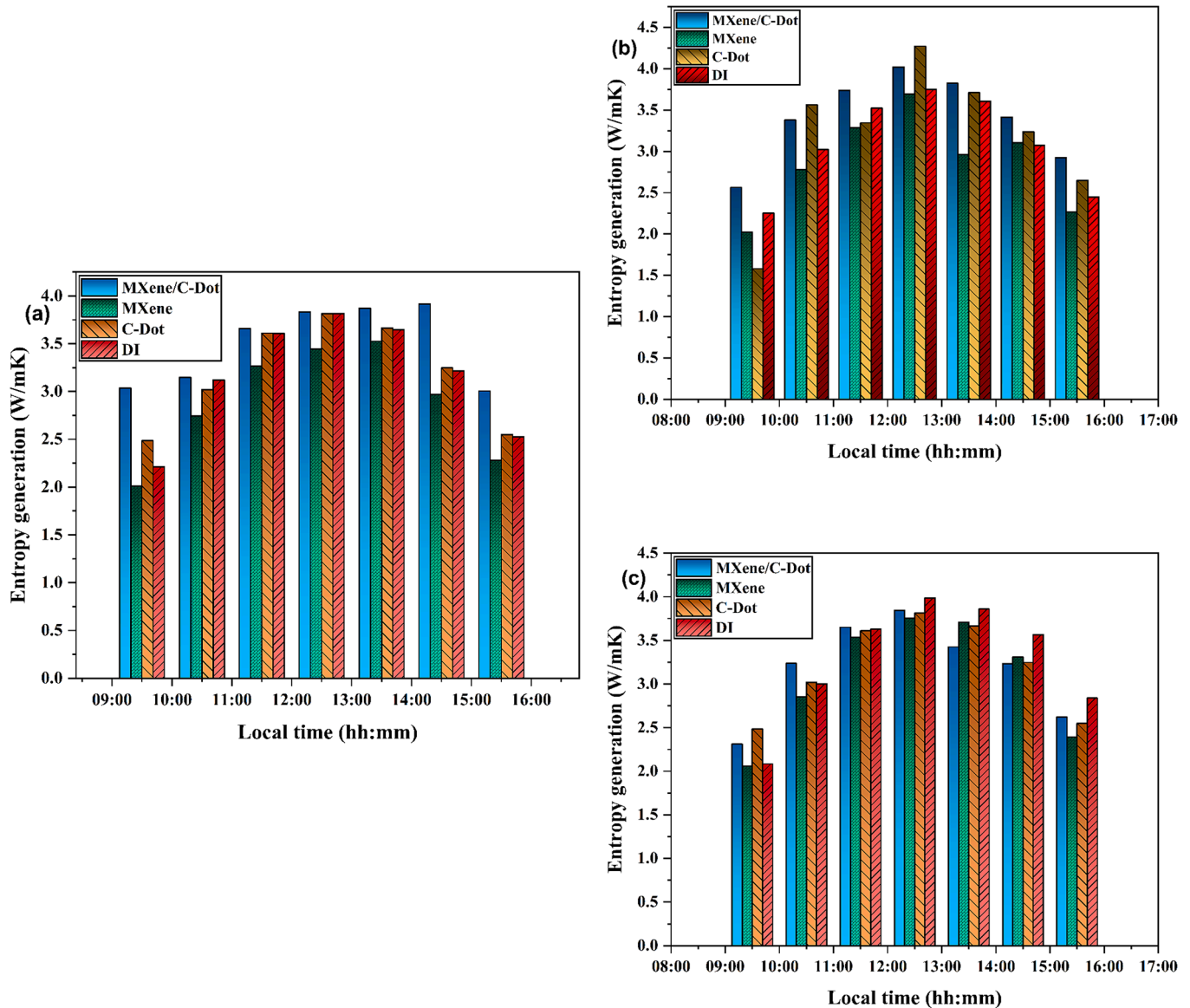
Fig. 20. Entropy generation in DAPTC at (a) 0.2 lpm, (b) 0.6 lpm, and (c) 1.2 lpm.

considerable enhancement in thermal efficiency over DI water. The thermal efficiency of DAPTC was found to be improved by 29.25 and 31.34 % with MXene and MXene/C-dot hybrid nanofluid. Fig. 18 (c) shows the thermal efficiency curves of DAPTC at a flow rate of 1.2 lpm. The highest efficiency of 50.5 % was obtained for the C-dot nanofluid at 1:00 pm when the irradiation was 816 Wm^{-2}. The highest efficiency reported with MXene/C-dot and MXene nanofluid is 47.5 % and 45.1 %, respectively. The thermal efficiency of the system increased by 36.8 %, 33.3 %, and 32.6 % with C-dot, hybrid and MXene nanofluids, respectively, in comparison to DI water at 1.2 lpm. The maximum, minimum, and average thermal efficiency of the system with each working fluid was summarized as shown in Table 5. The better photothermal conversion efficiency of C-dot nanofluid, in comparison to other fluids, is most probably due to the low scattering coefficient. As the scattering coefficient increases the percentage of irradiation absorbed by the fluid decreases. Another major reason is the fluorescence property of the C-dot nanofluid. As the photoluminescence efficiency increases, a major portion of the absorbed energy may be lost by re-emission. The scattering and photoluminescence of hybrid and MXene could be higher than C-dot nanofluid, which need to be established by

photoluminescence study in future stages of the research.

3.4.2. Impact on outlet temperature

The outlet temperature of the working fluids in the absorber tube for each flow rate is visualized in Fig. 19. The variation in outlet temperature with local time almost resembles the thermal efficiency curve. The outlet temperature is directly dependent on the incident solar radiation, and thermal efficiency of the system. The highest temperature was achieved at 0.2 lpm and the outlet temperature was found to decrease with an increase in flow rate and reached a minimum at 1.2 lpm. Fig. 19 (a) shows that the C-dot nanofluid is producing the highest temperature of 70.1℃ at the outlet. The temperature of MXene/C-dot nanofluid is almost coinciding with that of C-dot and exhibited a high value of about 69.77℃ at 1:00 pm. Even though the efficiency of the C-dot is higher than that of other fluids, the outlet temperature of MXene/C-dot nanofluid was higher at a few time intervals (09:30 – 10:am, and 2:30 – 3:30 pm). This increment was caused due to higher solar intensity during the mentioned time periods of the day, when hybrid nanofluid was tested. DI water showed the lowest temperature of about 42.2℃. The fluid outlet temperature at 0.6 lpm flow rate is shown in Fig. 19(b). A similar
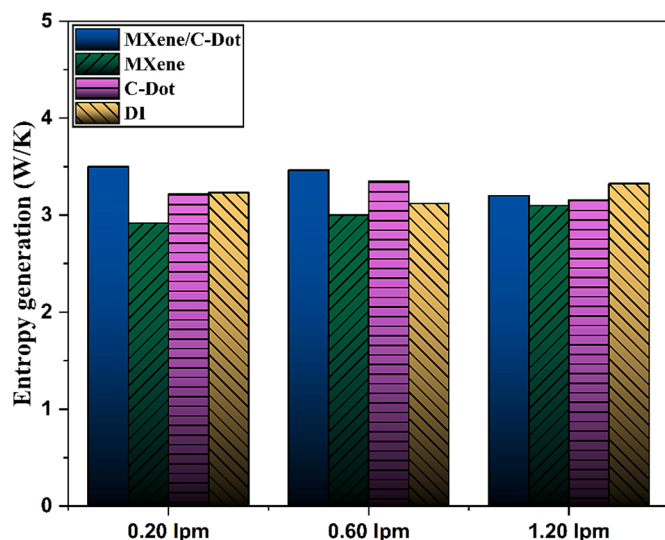
Fig. 21. Daily average entropy generation in DAPTC with (a) C-Dot, (b) MXene, and (c) MXene/C-Dot as the working fluid.

pattern as obtained for a flow rate of 0.2 lpm was observed in this case. The highest outlet temperature recorded was 46.6°C and was achieved by C-dot nanofluid. The maximum temperature obtained by MXene/C-dot, MXene and DI water was 43.95, 42.1, and 35.2°C, respectively. As seen in Fig. 19(c), a similar pattern in outlet temperature could be observed at a 1.2 lpm flow rate. The fluid temperature was considerably reduced. The maximum temperature attained by C-dot, MXene/C-dot, MXene and DI water was found to be 38.05, 38.81, 36.9, and 33.1°C, respectively. The thermal conductivity, stability and SWAF characterization value of optimized nanofluids as observed from Fig. 10(d) confirms the above conclusion. The combined effect of high SWAF and stability retention property of C-dot and hybrid has significantly contributed to the enhanced photothermal efficiency over MXene and DI water. Also, the average, maximum and minimum values of outlet temperature of different HTFs at all flow rates are provided in Table 5.

3.4.3. Entropy generation analysis

Entropy generation in the system with each fluid during the operational time is shown in Fig. 20 (a), (b) and (c). Results show that the total entropy production in the system increases with time and attains maximum value during noon. During noon time the solar intensity reaches a maximum resulting in an increase in the heat loss and consequently the irreversibility associated with the system increases. As inferred from Eq. (10), the major contributors in the entropy generation process are the irreversibilities during the photothermal energy conversion, and during heat loss to the surrounding. The irreversibility due to photothermal conversion was found to be the dominant one, and the value was observed to increase with time and reached a maximum value at highest irradiation. This was due to the fact that photothermal conversion was directly related to irradiation intensity. At the meantime, the irreversibility due to heat loss also experienced a similar trend, as the heat lost to the ambient increased with increase in irradiation. The highest entropy generated by the system with MXene/C-dot, MXene, C-dot and DI water was about 4.5, 3.78, 4.43, and 4.0 WK^{-1}. Entropy generation was observed to be higher for MXene, and C-dot based system in comparison to other fluids, as the irreversibility due to photothermal conversion was higher due to higher photothermal efficiency. In the case of DI water, the entropy production contributed by heat loss from the system was considerable. Its id observed from the Fig. 20, that the entropy generation peaked for each fluid when the flow rate was 0.6 lpm. It is to be noted that even though the thermal efficiency of the system with nanofluids and base fluid was observed to be maximum at

highest flow rate of 1.2 lpm, and the heat loss was maximized at very low flow rate of 0.2 lpm, the maximum entropy generation occurred at medium flow rate of 0.6 lpm. This shows that the combined effect of photothermal efficiency, and heat transfer to the ambient has a greater influence on the irreversibilities of the system. The average entropy generation during each case is depicted in Fig. 21. It is inferred that the entropy generation of DI-based DAPTC was higher than nanofluids only at 1.2 lpm. The entropy generation in the system with each working fluids was tabulated as shown in Table 5.

4. Conclusions

Photothermal application of MXene, C-dot and hybrid nanofluid in a DAPTC was investigated for the first time in this study. Nanofluids were synthesized and thermo-optical, stability and corrosion characterizations were conducted. The concentration of nanofluids was optimized based on solar absorption percentage, thermal conductivity, and stability degradation rate. Optimized concentration of C-dot, MXene, and hybrid nanofluids was calculated to be 0.15, 0.1, and 0.15 wt%. Solar weighted absorption study shows that C-dot nanofluid exhibited absorption in the UV spectral range, while absorption by MXene nanofluid peaked in the visible and NIR spectrum. MXene/C-dot hybrid nanofluid was observed to be showing complementary spectral absorption properties of C-dot and MXene nanofluids. Corrosion and stability analysis performed on the nanofluids shows that hybrid nanofluid poses less corrosion to copper in comparison to DI water and C-dot nanofluid. Tafel slope shows that the corrosion rate of copper in hybrid nanofluid is the least, causing annual corrosion of 0.6 mm/year with 64.5 % anticorrosive efficiency over DI water. An experimental investigation was conducted on DAPTC at outdoor climatic conditions of Calicut, Kerala. The performance of the system was analysed based on thermal efficiency and entropy generation analysis. Hybrid and C-dot nanofluid recorded the highest thermal efficiencies of 47.5 and 50.5 %, respectively at 0.2 lpm flow rate. The results show that a synergistic effect of thermal conductivity, stability, and SWAF contributes to the photothermal efficiency enhancement, rather than one dominant parameter. Exergy study on DAPTC showed that entropy generation of the system with hybrid, MXene, and C-dot was around 4.5, 3.78, and 4.43 WK^{-1}, respectively. Entropy generation of hybrid, C-dot, and MXene nanofluids was contributed due to irreversibility arising from photothermal energy conversion, while for DI water the entropy generation from heat loss was considerably higher due to poor photothermal efficiency. In a nutshell, this study shows that hybrid MXene/C-dot nanofluid with exceptional thermal stability, improved corrosion resistance, and significant photothermal conversion efficiency proves to be a better optical fluid for DASCs, in comparison to other nanofluids and base fluid.

Declaration of competing interest

The authors declare that they have no known competing financial interests or personal relationships that could have appeared to influence the work reported in this paper.

Appendix A. Supplementary data

Supplementary data to this article can be found online at https://doi.org/10.1016/j.solener.2024.112317.

References

[1] Ş. Kılkış, G. Krajačić, N. Duić, M.A. Rosen, M.A. Al-Nimr, Effective mitigation of climate change with sustainable development of energy, water and environment systems, Energy Convers. Manag. 269 (2022), https://doi.org/10.1016/j.enconman.2022.116146.

[2] A. Azarpour, O. Mohammadzadeh, N. Rezaei, S. Zendehboudi, Current status and future prospects of renewable and sustainable energy in North America: progress and challenges, Energy Convers. Manag. 269 (2022) 115945, https://doi.org/10.1016/j.enconman.2022.115945.

[3] S. Sreekumar, N. Shah, J.D. Mondol, N. Hewitt, S. Chakrabarti, Numerical investigation and feasibility study on mxene/water nanofluid based photovoltaic/thermal system, Clean. Energy Syst. 2 (2022) 100010, https://doi.org/10.1016/j.cles.2022.100010.

[4] X. Zuo, L. Song, W. Yang, Z. Zhang, X. Gao, J. Zhan, S. Wu, X. Wang, W. Zhu, H. Li, D. Zhang, H. Yin, H. Yan, Y. An, Silicon dioxide coating nanocomposites and cellulose-based stable nanofluid for direct absorption solar collection, Sol. Energy. 262 (2023) 111797, https://doi.org/10.1016/j.solener.2023.111797.

[5] G. Mittelman, A. Kribus, M. Epstein, B. Lew, S. Baron, Y. Flitsanov, H. Vitoshkin, Solar spectral beam splitting for photochemical conversion and polygeneration, Energy Convers. Manag. 258 (2022) 115525, https://doi.org/10.1016/j.enconman.2022.115525.

[6] Y. Jiao, Z. Wang, L. Liu, X. Liu, X. Pan, G. Li, Q. Zhang, C. Lu, C. He, Numerical simulation of the interaction and coalescence of inline hydrogen bubbles in biohydrogen production by photofermentation with corncob, Int. J. Hydrogen Energy. (2023), https://doi.org/10.1016/j.ijhydene.2023.02.064.

[7] W. Gu, X. Wang, H. Lu, M. Mutailipu, Energy and exergy analyses of a bifacial photovoltaic/thermal system with nanofluids, Sol. Energy. 262 (2023) 111875, https://doi.org/10.1016/j.solener.2023.111875.

[8] M. Motamedi, G. Jia, Y. Yao, K. Shanks, P. Yousefi, Y.L. Hewakuruppu, M. Rafeie, F. Lindner, R. Patterson, S. Christiansen, J. Plentz, P. Koshy, R.A. Taylor, Nanopatterned indium tin oxide as a selective coating for solar thermal applications, Renew. Energy. 210 (2023) 386–396, https://doi.org/10.1016/j.renene.2023.04.020.

[9] S. Sreekumar, N. Shah, J.D. Mondol, N. Hewitt, S. Chakrabarti, Broadband absorbing mono, blended and hybrid nanofluids for direct absorption solar collector: a comprehensive review, Nano Futur. (2022), https://doi.org/10.1088/2399-1984/ac57f7.

[10] S. Kumar, N. Chander, V.K. Gupta, R. Kukreja, Progress, challenges and future prospects of plasmonic nanofluid based direct absorption solar collectors – a state-of-the-art review, Sol. Energy. 227 (2021) 365–425, https://doi.org/10.1016/j.solener.2021.09.008.

[11] L. Xing, Y. Ha, R. Wang, Z. Li, Recent advances of solar thermal conversion with wide absorption spectrum based on plasmonic nanofluids, Sol. Energy. 262 (2023) 111858, https://doi.org/10.1016/j.solener.2023.111858.

[12] X. Zhao, X. Han, Y. Yao, J. Huang, Stability investigation of propylene glycol-based Ag@SiO2 nanofluids and their performance in spectral splitting photovoltaic/thermal systems, Energy 238 (2022) 122040, https://doi.org/10.1016/j.energy.2021.122040.

[13] L. Das, K. Habib, K. Irshad, R. Saidur, S. Algarni, T. Alqahtani, Thermo-optical characterization of therminol55 based MXene–Al2O3 hybridized nanofluid and new correlations for thermal properties, Nanomaterials 12 (2022), https://doi.org/10.3390/nano12111862.

[14] Z. Li, A. Kan, K. Wang, Y. He, N. Zheng, W. Yu, Optical Properties and photothermal conversion performances of graphene based nanofluids, Appl. Therm. Eng. 203 (2021) 117948, https://doi.org/10.1016/j.applthermaleng.2021.117948.

[15] H. Guo, W. Liu, Q. Shu, H. Zhu, J. Yang, L. Xiao, Full-spectrum photo-thermal conversion of plasmonic LaB6 nanofluids, Mater. Lett. 308 (2022) 131261, https://doi.org/10.1016/j.matlet.2021.131261.

[16] W. Zhu, X. Zuo, Y. Ding, Y. An, W. Yang, Experimental comparison of the photothermal conversion performance of coal and plant soot nanofluids for direct absorption solar collectors, Sol. Energy. 264 (2023) 112056, https://doi.org/10.1016/j.solener.2023.112056.

[17] B.V. Balakin, P.G. Struchalin, Eco-friendly and low-cost nanofluid for direct absorption solar collectors, Mater. Lett. 330 (2022) 133323, https://doi.org/10.1016/j.matlet.2022.133323.

[18] G. Jiang, W. Yu, H. Lei, Novel solar membrane distillation system based on Ti 3 C 2 T X MXene nanofluids with high photothermal conversion efficiency, Desalination 539 (2022) 115930, https://doi.org/10.1016/j.desal.2022.115930.

[19] A. Joseph, S. Sreekumar, C.S.S. Kumar, S. Thomas, Optimisation of thermo-optical properties of SiO2/Ag–CuO nanofluid for direct absorption solar collectors, J. Mol. Liq. (2019) 111986, https://doi.org/10.1016/j.molliq.2019.111986.

[20] J. Wen, Q. Chang, J. Zhu, R. Cui, C. He, X. Yan, X. Li, The enhanced photothermal characteristics of plasmonic ZrC/TiN composite nanofluids for direct absorption solar collectors, Renew. Energy. 206 (2023) 676–685, https://doi.org/10.1016/j.renene.2023.02.095.

[21] J. Yu, D. Zhu, C. Qi, W. Zhang, Photothermal characteristic and evaporation efficiency of core-shell Ag@Fe3O4 nanofluids, Powder Technol. 422 (2023) 118464, https://doi.org/10.1016/j.powtec.2023.118464.

[22] S. Sreehari, A. Joseph, S. Thomas, Development of a low cost nanofluid based direct absorption solar collector, Mater. Today Proc. 22 (2019) 2424–2430, https://doi.org/10.1016/j.matpr.2020.03.368.

[23] M.M. Heyhat, M. Valizade, S. Abdolahzade, M. Maerefat, Thermal efficiency enhancement of direct absorption parabolic trough solar collector (DAPTSC) by using nanofluid and metal foam, Energy 192 (2020) 116662, https://doi.org/10.1016/j.energy.2019.116662.

[24] A. Joseph, S. Thomas, Energy, exergy and corrosion analysis of direct absorption solar collector employed with ultra-high stable carbon quantum dot nanofluid, Renew. Energy. 181 (2022) 725–737, https://doi.org/10.1016/j.renene.2021.09.079.

[25] X. Chen, Z. Xiong, M. Chen, P. Zhou, Ultra-stable carbon quantum dot nanofluids for direct absorption solar collectors, Sol. Energy Mater. Sol. Cells. 240 (2022) 111720, https://doi.org/10.1016/j.solmat.2022.111720.

[26] S. Farooq, C.V.P. Vital, G. Tikhonowski, A.A. Popov, S.M. Klimentov, L.A. G. Malagon, R.E. de Araujo, A.V. Kabashin, D. Rativa, Thermo-optical performance of bare laser-synthesized TiN nanofluids for direct absorption solar collector applications, Sol. Energy Mater. Sol. Cells. 252 (2023) 112203, https://doi.org/10.1016/j.solmat.2023.112203.

[27] S. Sreekumar, A. Joseph, C.S. Sujith Kumar, S. Thomas, Investigation on influence of antimony tin oxide/silver nanofluid on direct absorption parabolic solar collector, J. Clean. Prod. 249 (2020) 119378, https://doi.org/10.1016/j.jclepro.2019.119378.

[28] J. Qu, G. Zhou, M. Zhang, L. Shang, W. Yu, Effect of reverse irradiation angle on the photo-thermal conversion performance of MXene nanofluid-based direct absorption solar collector, Sol. Energy Mater. Sol. Cells. 251 (2023) 112164, https://doi.org/10.1016/j.solmat.2022.112164.

[29] Z. Bao, N. Bing, X. Zhu, H. Xie, W. Yu, Ti3C2Tx MXene contained nanofluids with high thermal conductivity, super colloidal stability and low viscosity, Chem. Eng. J. 406 (2021) 126390, https://doi.org/10.1016/j.cej.2020.126390.

[30] A. Joseph, S. Sreekumar, S. Thomas, Energy and exergy analysis of SiO2/Ag-CuO plasmonic nanofluid on direct absorption parabolic solar collector, Renew. Energy. 162 (2020) 1655–1664, https://doi.org/10.1016/j.renene.2020.09.139.

[31] S. Sreekumar, A. Ganguly, S. Khalil, S. Chakrabarti, N. Hewit, J.D. Mondol, N. Shah, Thermo-optical characterization of novel MXene/Carbon-dot hybrid nanofluid for heat transfer applications, J. Clean. Prod. (2024) 140395, https://doi.org/10.1016/j.jclepro.2023.140395.

[32] H.S. Moghaieb, V. Amendola, S. Khalil, S. Chakrabarti, P. Maguire, D. Mariotti, Nanofluids for direct-absorption solar collectors—DASCs: a review on recent progress and future perspectives, Nanomaterials 13 (2023), https://doi.org/10.3390/nano13071232.

[33] A.A. Khan, A.A. Razin, D.-S.-S. Ahammed, M.S. Kaiser, Comparison of electrochemical corrosion performance of eutectic Al-Si automotive alloy in deep seawater and 3.5% NaCl solution, Mater. Today Proc. (2023) 1–7, https://doi.org/10.1016/j.matpr.2023.01.179.

[34] H. Li, E. Zhou, D. Zhang, D. Xu, J. Xia, C. Yang, H. Feng, Z. Jiang, X. Li, T. Gu, K. Yang, Microbiologically influenced corrosion of 2707 hyper-duplex stainless steel by marine pseudomonas aeruginosa biofilm, Sci. Rep. 6 (2016) 1–12, https://doi.org/10.1038/srep20190.

[35] M. Stern, A.L. Geaby, Electrochemical polarization, J. Electrochem. Soc. 104 (1957) 56, https://doi.org/10.1149/1.2428496.

[36] M. Salehi, M. Mozammel, S.M. Emarati, Superhydrophobic and corrosion resistant properties of electrodeposited Ni-TiO2/TMPSi nanocomposite coating, Colloids Surfaces A Physicochem. Eng. Asp. 573 (2019) 196–204, https://doi.org/10.1016/j.colsurfa.2019.04.024.

[37] S. Yu, H. Jin, M. Cao, Study on corrosion characteristic of semi-ring steel plate for strengthening shield tunnel under DC stray current, Constr. Build. Mater. 347 (2022) 128631, https://doi.org/10.1016/j.conbuildmat.2022.128631.

[38] A. Joseph, V. Gautham, K.S. Akshay, V. Sajith, 2D MoS2-hBN hybrid coatings for enhanced corrosion resistance of solid lubricant coatings, Surf. Coatings Technol. 443 (2022) 128612, https://doi.org/10.1016/j.surfcoat.2022.128612.

[39] C. Cui, A. Chen, Z. Pan, R. Ma, Two-dimensional numerical model and fast estimation method for calculating crevice corrosion of cross-sea bridges, Constr. Build. Mater. 206 (2019) 683–693, https://doi.org/10.1016/j.conbuildmat.2019.02.103.

[40] A. Poursaee, Potentiostatic transient technique, a simple approach to estimate the corrosion current density and Stern-Geary constant of reinforcing steel in concrete, Cem. Concr. Res. 40 (2010) 1451–1458, https://doi.org/10.1016/j.cemconres.2010.04.006.

[41] J. He, J. Sun, Y. Meng, F. Yang, H. Tang, MoS2–Al2O3 nanofluid-induced microstructure evolution and corrosion resistance enhancement of hot-rolled steel surface, J. Mater. Sci. 56 (2021) 17805–17823, https://doi.org/10.1007/s10853-021-06415-x.

[42] H. Tang, J. Sun, X. Yan, P. Wu, Electrochemical and adsorption behaviors of thiadiazole derivatives on the aluminum surface, RSC Adv. 9 (2019) 34617–34626, https://doi.org/10.1039/c9ra05740d.

[43] R. Goyal, K.S. Reddy, Numerical investigation of entropy generation in a solar parabolic trough collector using supercritical carbon dioxide as heat transfer fluid, Appl. Therm. Eng. 208 (2022) 118246, https://doi.org/10.1016/j.applthermaleng.2022.118246.

[44] R.J. Moffat, Describing the uncertainties in experimental results, Exp. Therm. Fluid Sci. 1 (1988) 3–17, https://doi.org/10.1016/0894-1777(88)90043-X.

[45] M. Hosseinzadeh, M. Sardarabadi, M. Passandideh-Fard, Energy and exergy analysis of nanofluid based photovoltaic thermal system integrated with phase change material, Energy 147 (2018) 636–647, https://doi.org/10.1016/j.energy.2018.01.073.

[46] X. Cui, Q. Ruan, X. Zhuo, X. Xia, J. Hu, R. Fu, Y. Li, J. Wang, H. Xu, Photothermal nanomaterials: a powerful light-to-heat converter, Chem. Rev. 123 (2023) 6891–6952, https://doi.org/10.1021/acs.chemrev.3c00159.

[47] Y. Song, G. Jiang, Y. Chen, P. Zhao, Y. Tian, Effects of chloride ions on corrosion of ductile iron and carbon steel in soil environments, Sci. Rep. 7 (2017) 1–13, https://doi.org/10.1038/s41598-017-07245-1.

[48] B.G. Prakashaiah, D. Vinaya Kumara, A. Anup Pandith, A. Nityananda Shetty, B. E. Amitha Rani, Corrosion inhibition of 2024–T3 aluminum alloy in 3.5% NaCl by thiosemicarbazone derivatives, Corros. Sci. 136 (2018) 326–338, https://doi.org/10.1016/j.corsci.2018.03.021.